PNAS RESEARCH ARTICLE | CELL BIOLOGY
BIOPHYSICS AND COMPUTATIONAL BIOLOGY

The kinetochore corona orchestrates chromosome congression through transient microtubule interactions

Christopher E. Miles[a,1,2], Fioranna Renda[b,1], Irina Tikhonenko[b], Angus Alfieri[b], Alex Mogilner[c,d], and Alexey Khodjakov[b]

Affiliations are included on p. 12.

Edited by Kerry Bloom, The University of North Carolina, Chapel Hill, NC; received September 2, 2025; accepted December 23, 2025

For proper segregation of chromosomes and successful cytokinesis, chromosomes must first "congress"—gather in a tight plate near the spindle equator. Molecular mechanism(s) of congression are not fully understood. Here we combine live-cell microscopy, perturbations of microtubule motor activities, correlative light/electron microscopy, and computational modeling, to quantitatively characterize the early-prometaphase movements that bring the scattered chromosomes to the equator in human RPE1 cells. We find that the early-prometaphase movements are directed toward the center of the spindle axis and not the spindle poles. Centromere velocity of the centripetal movements is not constant, with centromeres moving faster at larger distances from the spindle center. We also detect that numerous short microtubules appear at kinetochores at the earliest stages of spindle assembly and prior to chromosome congression. Computational modeling reveals that a mechanism based on brief, stochastic, minus-end directed interactions between the short microtubules protruding from the kinetochores and long appropriately curved microtubules within the spindle accurately predicts the observed distance-velocity function. Further, the model predicts that insufficient numbers of microtubules protruding from the kinetochores decreases the velocity and randomizes directionality of congression movements. These predictions match changes in the chromosome behavior observed in cells with suppressed nucleation of microtubules at the kinetochore corona (RPE1 Rod$^{\Delta/\Delta}$). In contrast, predictions of computational models based on continuous pulling forces at kinetochores differ significantly from the experimental observations. Together, live-cell observations and modeling reveal a mechanism that enables the efficient and synchronized arrival of chromosomes to the spindle equator.

mitosis | spindle assembly | chromosomes | prometaphase | computational modeling

Equal segregation of chromosomes into the two daughter cells during mitosis is enacted by the "mitotic spindle," a self-assembling macromolecular machine comprising thousands of microtubules (MTs) (1–3). The two sister chromatids move to the opposite spindle poles by forces acting along MTs attached to the "kinetochores," macromolecular complexes residing on the opposite sides of chromosome's "centromere." MTs attached to kinetochores form bundles of uniform polarity ("K-fibers") with MT plus ends residing at the kinetochore (4). Two mechanisms of K-fiber formation have been identified. In one, a kinetochore attaches to MTs produced by a spindle pole, which instantly establishes a direct connection with the pole (5). Alternatively, kinetochores grab MTs nucleated in their immediate proximity and the connection to the pole is mediated by interactions between the distal (minus) ends of short MTs protruding from the kinetochore (skMTs) and other MTs within the spindle (1, 6–8).

Formation of simultaneous connections between sister kinetochores and the opposite spindle poles (termed amphitelic attachment) is most efficient when centromeres reside near the spindle equator equidistant to the poles (9). In contrast, near a spindle pole establishing connection to the distal pole is impeded and the probability of simultaneous attachment of both kinetochores to the same pole (termed "syntelic attachment") increases. Thus, conditions that promote accumulation of chromosomes near spindle poles (termed "monoorientation") decrease the fidelity of chromosome segregation and adversely affect the progeny (10, 11). Thus, a major goal of spindle assembly is to rapidly gather the initially scattered chromosomes in a tight group at the spindle equator. Molecular mechanism(s) that drive this gathering (termed "chromosome congression") are not well understood (12). Here, we combine quantitative analysis of chromosome behavior during early stages of spindle assembly (prometaphase), correlative light/electron microscopy (CLEM) reconstructions, and computational modeling to reveal these mechanisms. Our analyses suggest that direct kinetochore attachments to MTs produced by spindle poles are infrequent and the rapid chromosome congression during early prometaphase is driven

Significance

For equal segregation into daughter cells, chromosomes, scattered in a large volume at the onset of cell division, must congress into a narrow plate near the equator of the mitotic spindle. Molecular mechanisms of congression remain obscure. Here we use live-cell microscopy and structural analyses to quantitatively characterize chromosome behavior during congression in human cells. From these quantifications, we derive a computational model that accurately predicts directionality and velocity of chromosome movement, and suggests that the force arises from stochastic, transient, minus-end directed interactions between short microtubules protruding from the kinetochores and long appropriately shaped microtubules within the spindle. The model also accurately predicts changes in chromosome behavior in cells with functionally deficient kinetochores.

Author contributions: C.E.M., F.R., A.M., and A.K. designed research; C.E.M., F.R., I.T., A.A., and A.K. performed research; C.E.M., F.R., I.T., A.A., A.M., and A.K. analyzed data; and C.E.M., F.R., A.M., and A.K. wrote the paper.

The authors declare no competing interest.

This article is a PNAS Direct Submission.

[1] C.E.M. and F.R. contributed equally to this work.

[2] To whom correspondence may be addressed. Email: chris.miles@utah.edu.

This article contains supporting information online at https://www.pnas.org/lookup/suppl/doi:10.1073/pnas.2524367123/-/DCSupplemental.

primarily by highly dynamic interactions between skMTs and long, properly shaped, antiparallel MTs within the spindle. The force generated by these interactions is directed toward the minus ends of spindle MTs, which suggests involvement of cytoplasmic dynein. Importantly, our computational model accurately predicts measurable changes in early-prometaphase chromosome behavior, including attenuated velocity of centromere movements and the rate of monoorientation corrections that occur in cells with a lower number of skMTs. This represents a significant step toward a quantitative, predictive understanding of mitotic spindle assembly in human cells.

Results

Early-Prometaphase Decrease in Monooriented Chromosomes Depends on the Kinetochore Corona but Not Kinetochore Plus-End Directed Motor Activity. In human somatic cells, the mitotic spindle principally comprises two asters of MTs that emanate from the spindle poles and overlap in the middle (Fig. 1*A* and *SI Appendix*, Fig. S1*A*). In this architecture, chromosomes near the spindle equator (termed "bioriented") attach simultaneously to MTs emanating from both spindle poles (termed "amphitelic attachment"), which is necessary for proper segregation. In contrast, formation of amphitelic attachments on "monooriented" chromosomes, near a spindle pole, is improbable due to the lower number of MTs from the distal pole (Fig. 1*A*). These chromosomes then need to congress closer to the equator (Fig. 1*B*).

The spindle assembly initiates when the NEB enables direct contacts between the chromosomes and MTs. At NEB, chromosomes are uniformly scattered within the nuclear volume shaped as a discoid with the shorter axis orthogonal and longer axis parallel to the substrate. Two centrosomes, whose MT nucleating activities define the spindle poles, reside consistently on the opposite sides of the nucleus within invaginations of the nuclear envelope (*SI Appendix*, Fig. S1*A*, NEB). In cells where centrosomes are separated at NEB along the longer nuclear axis, the spindle axis remains roughly parallel to the substrate and the length of the spindle is relatively constant throughout mitosis. Although infrequent [~25% of RPE1 (13, 14)], these cells offer a stable viewpoint on the chromosome behavior throughout prometaphase (*SI Appendix*, Fig. S1*B*). Conventional microscopy reveals that the separation between the centrosomes and chromosomes increases progressively after NEB (Fig. 1*C*). In less than 3 min, most chromosomes clear the monoorientation zones near spindle poles (Fig. 1*C*, 2:20) and only occasionally individual chromosomes transiently approach the poles at later times (Fig. 1*C*, 4:30). Kinetochores rapidly gather from a scattered cloud into a tight equatorial plate (Fig. 1*C*).

In most cells (~75% in RPE1), the centrosomes separate along the shorter nuclear axis so that the spindle initially is nearly orthogonal to the substrate but subsequently rotates to nearly parallel to the substrate by mid-late prometaphase (9, 13, 14). In these cells, chromosome movements within the spindle are obscured by the constantly changing viewpoint (*SI Appendix*, Fig. S1*C*). While chromosomes often appear near poles in the conventional projections onto XY-plane (*SI Appendix*, Fig. S1*C*), 3-D visualization reveals that the distance between chromosomes and the poles progressively increases (Fig. 1*D*) akin to cells with steadily horizontal spindle orientation.

To uncouple chromosome behavior within the spindle from changes in the spindle orientation within the cell, we express positions of chromosomes' centromeres (defined here as the midpoint

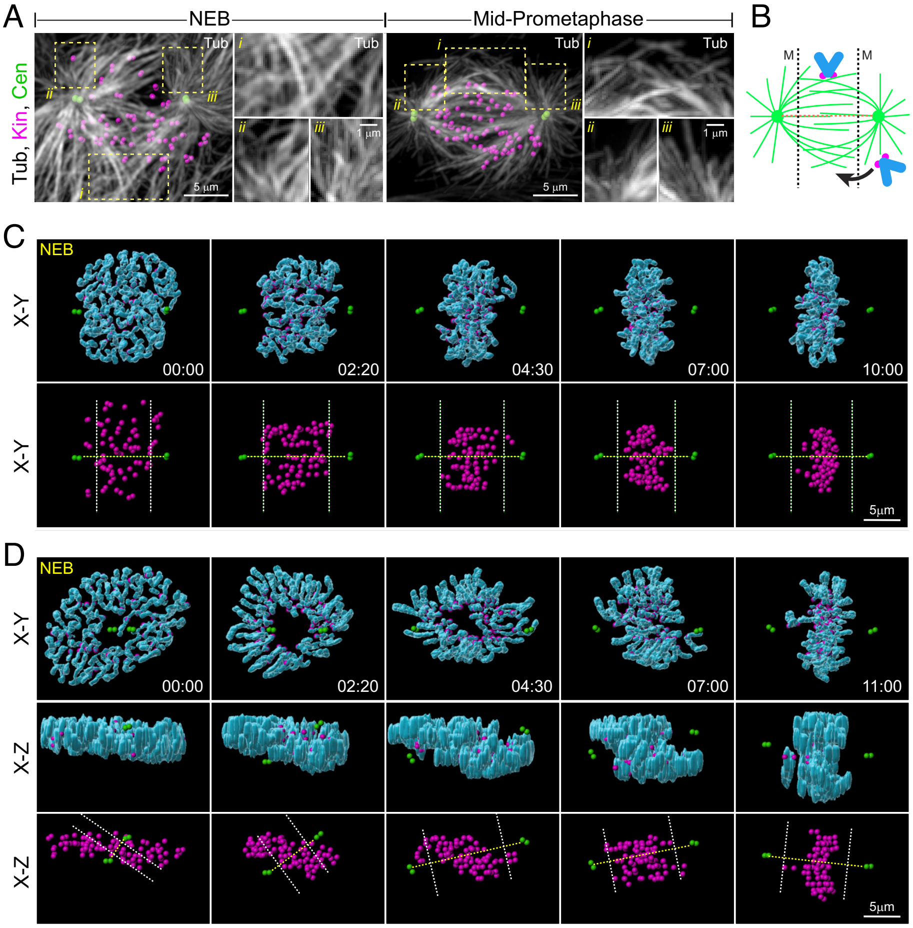

Fig. 1. Formation of metaphase plate in RPE1 cells with steadily horizontal or gradually rotating spindle. (*A*) Distribution of MTs and centromeres at nuclear envelope breakdown (NEB) and mid-prometaphase. Maximum-intensity projections of the entire cell. *Insets* show higher magnification of labeled areas. i) Overlapping MTs near the spindle equator, ii) and iii) radial microtubule arrays near spindle poles. MTs (white), centrioles (green), and kinetochores (magenta) are shown. (*B*) Cartoon of the spindle during prometaphase. Chromosomes near the equator encounter MTs from both poles, whereas near the spindle poles MTs from the distal pole are rare. Dashed lines denote parts of the spindle where chromosomes are monooriented. (*C* and *D*) Changes in spatial distribution of chromosomes during prometaphase in cells with steadily horizontal (*C*) or rotating (*D*) spindle. The volumes are aligned at each time point to stabilize XYZ position of the spindle center and spindle orientation in XY (but not in XZ) projections. Centrosomes are on the opposite sides of the nucleus along the longer (*C*) or shorter (*D*) axis of the discoid nucleus at NEB. Chromosomes rapidly void monoorientation zones (outside of dashed white lines). Dashed yellow lines denote the spindle axis. Chromosome arms are segmented and surface-rendered (blue). Balls mark positions of kinetochores (magenta) and centrioles (green). Timestamps are in minutes:seconds.

between sister kinetochores) in a cylindrical coordinate system defined by the distance to the spindle axis (ρ), distance to the spindle equator (Z), and angle between the horizon and the vector from the center of the spindle axis (hereafter, spindle center) to the centromere (θ) (*SI Appendix*, Fig. S2*A*). This isolates the axial (parallel to the spindle axis) and equatorial (parallel to the equatorial plane) components of centromere movements. Further, by normalizing Z values to the spindle length, we can directly compare centromere behavior within the monoorientation (<1/3 of the half-spindle length from a pole) and biorientation zones (*SI Appendix*, Fig. S2*A*).

Due to the initial position of centrosomes within invaginations of the nuclear envelope, ~40% of centromeres in RPE1 cells (358 of 876 tracked in 19 cells) are monooriented at NEB. Indeed, many centromeres are farther from the equator than the centrosomes at this stage (Fig. 2*A*). The number of the inherently monooriented polar centromeres decreases rapidly from ~20 to ~2 per cell in the first 400 s of prometaphase (Fig. 2*B*, RPE1) and the correction involves movement of centromeres closer to the equator (Fig. 2*C*, RPE1). In contrast, inherently equatorial centromeres rarely become monooriented later in prometaphase (Fig. 2 *A* and *B*, RPE1) and their mean distance to the equator remains relatively constant (Fig. 2*C*, RPE1). To test whether the changes in distribution of polar centromeres require motor activity, we use 20-nM GSK923295 to inhibit CENP-E, the only plus-end directed kinesin at the kinetochore (15). CENP-E inhibition does not largely affect the decrease in monooriented chromosomes during the first 400 s of prometaphase (Fig. 2*B*, RPE1 CENP-E-inh). Later, the number of monooriented centromeres increases in CENP-E-inhibited RPE1 as some already-congressed chromosomes reposition closer to the spindle poles. Both polar and equatorial centromeres contribute to this process at the same rate (Fig. 2 *B* and *C*, RPE1 CENP-E-inh) and cumulatively >25% of chromosomes (13 ± 6 per cell) become monooriented 13 to 15 min after NEB. This level of monoorientation indicates that CENP-E activity is significantly suppressed in 20-nM GSK923295. To verify, we track kinetochore movements in cells depleted for CENP-E via siRNA (8). Both the initial decrease and subsequent accumulation of monooriented chromosomes in these cells are similar to cells treated with 20-nM GSK923295 (*SI Appendix*, Fig. S3 *A* and *B*). Thus, while CENP-E is necessary to avoid accumulation of monoorientation during mid- and late prometaphase, the initial relocation of most polar centromeres closer to the equator occurs independently of a plus-end directed motor activity at the kinetochore.

Monooriented chromosomes are known to become numerous when kinetochores lack the "fibrous corona," an outer-kinetochore complex involved in capturing spindle MTs as well as for nucleating noncentrosomal MTs near kinetochores (16–18). To assess monoorientation dynamics in the absence of the corona we use RPE1 Rod$^{\Delta/\Delta}$ cells (9, 19). In these cells, the number of polar

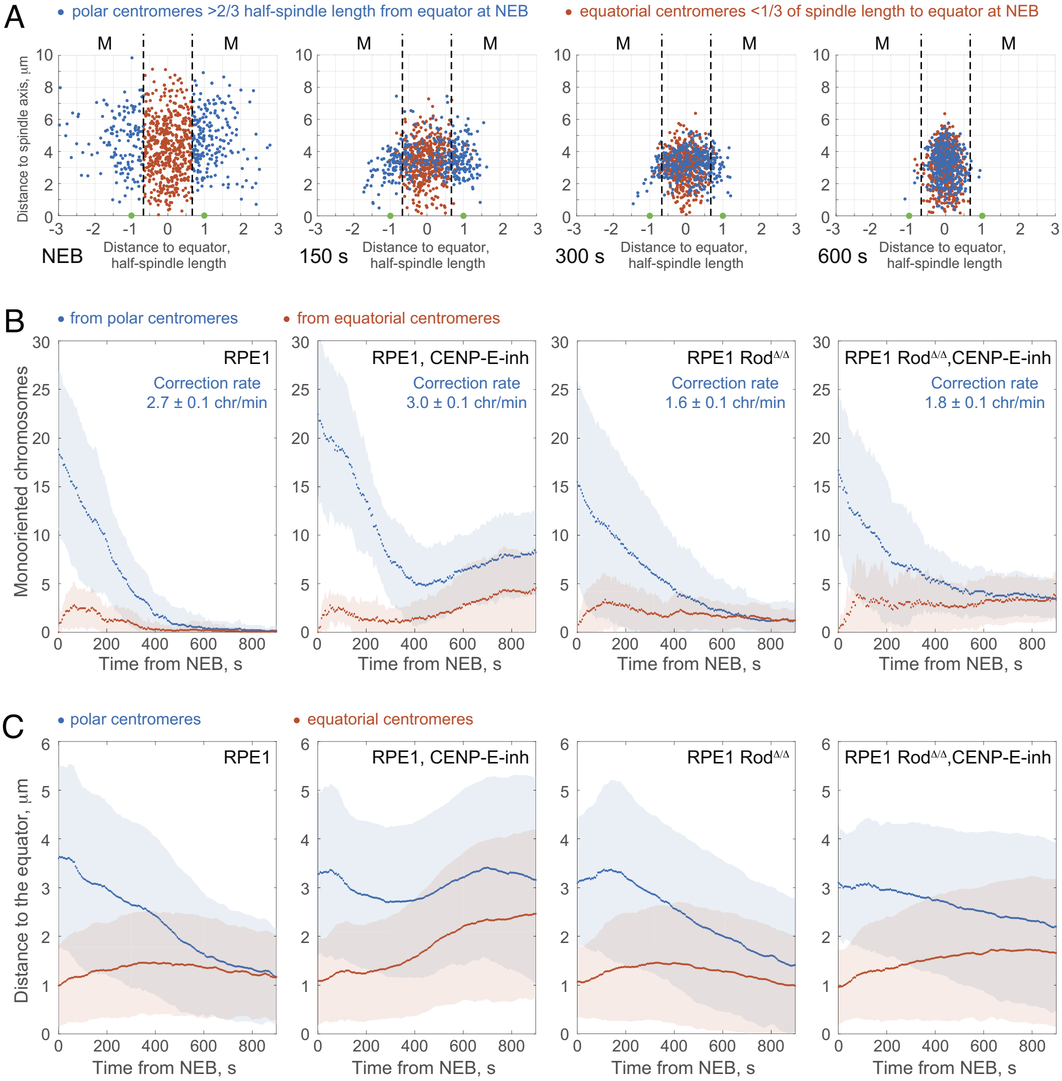

Fig. 2. Correction of chromosome monoorientation depends on the kinetochore corona but not on a plus-end directed motor activity. (*A*) Axial-radial Z-ρ distribution of centromeres during prometaphase in RPE1 cells (876 centromeres in 19 cells), with centrosomes marked in green. "Polar" centromeres (in monoorientation zones "M" at NEB), gradually relocate toward the equator, whereas initially "equatorial" centromeres rarely become monooriented. (*B*) Number of monooriented chromosomes (mean and SD per cell) from the polar (blue) and equatorial (orange) centromeres. "CENP-E-inh" cells were treated with 20-nM GSK923295. Monoorientation rates are slopes of linear fits from 5 to 60 s after NEB. (*C*) Mean (with SD) distance from the equator to polar (blue) and equatorial (orange) centromeres during prometaphase.

chromosomes decreases at a ~60% slower rate than in the wild-type RPE1, irrespective of CENP-E activity (Fig. 2*B*, Rod$^{\Delta/\Delta}$). Further, congression of the initially polar centromeres is significantly delayed in Rod$^{\Delta/\Delta}$ cells with active CENP-E. The initially equatorial centromeres maintain their equatorial position as in RPE1 cells (Fig. 2 *B* and *C*). Unexpectedly, the number of monooriented chromosomes does not increase during later prometaphase in Rod$^{\Delta/\Delta}$ cells with inhibited CENP-E (Fig. 2*C*, Rod$^{\Delta/\Delta}$ CENP-E-inh). Thus, unlike in RPE1 cells, CENP-E appears to be dispensable for maintaining equatorial positions of already congressed centromeres in Rod$^{\Delta/\Delta}$ cells. A possible explanation is that the equatorial position is normally maintained via a tug-of-war between CENP-E and dynein within the kinetochore corona. As dynein is not recruited to the kinetochores in Rod$^{\Delta/\Delta}$ cells, CENP-E is no longer needed to counteract the dynein-produced poleward force.

Kinetochore Corona Facilitates Rapid Relocation of the Peripheral Centromeres Toward the Spindle Center. Investigations into chromosome congression usually focus on the distribution of chromosomes along the spindle axis. However, we find that during early prometaphase more prominent deviations from the initial centromere positions occur in the orthogonal direction. Shortly after NEB, centromeres gather around the spindle axis within a circular area with a ~4 μm radius. This compaction of the centromere distribution arises primarily from relocation of the peripheral centromeres that are initially positioned >4.5 μm from the axis (Fig. 3*A*). The mean distance to the spindle axis for this population decreases from 6.0 ± 1.1 μm at NEB to 3.5 ± 0.8 μm in the first 300 s (Fig. 3*B*, RPE1) while the inner centromeres, initially residing <4.5 μm from the axis, change their positions only slightly (Fig. 3*B*, mean distance 3.0 ± 1.0 μm at NEB vs. 2.9 ± 1.0 μm at 300 s). Inhibition of CENP-E (Fig. 3*B*, RPE1-CENP-E-inh) or siRNA depletion of this protein (*SI Appendix*, Fig. S3*C*) do not significantly change the dynamics of centromere gathering. In contrast, the inward relocation of peripheral centromeres is delayed in Rod$^{\Delta/\Delta}$ cells irrespective of CENP-E activity (Fig. 3*B*). In Rod$^{\Delta/\Delta}$, the mean distance to the spindle axis remains relatively constant for ~100 s and then decreases slower than in RPE1 (Fig. 3*B*). The inner centromeres also exhibit a different behavior in Rod$^{\Delta/\Delta}$ cells. The mean distance for these centromeres increases from 3.0 ± 1.0 μm at NEB to 3.6 ± 1.2 μm at 90 s and subsequently decreases to its NEB value 300 s later (Fig. 3*B*, Rod$^{\Delta/\Delta}$ and Rod$^{\Delta/\Delta}$ CENP-E-inh). Together, these observations suggest that the kinetochore corona but not a plus-end directed motor activity at the kinetochore brings the initially scattered centromeres closer to the spindle axis.

To characterize how the scattered chromosomes gather closer to the spindle axis we split the Z-ρ spindle map of centromere positions into small spatial bins and calculate the mean displacement vectors for all centromeres within each bin at various times of prometaphase. This approach reveals a striking difference in the predominant direction of centromere movements in RPE1 vs. Rod$^{\Delta/\Delta}$ cells (Fig. 3 *C* and *D*). In RPE1 cells, peripheral centromeres synchronously move toward the center of the spindle during early prometaphase (1 to 2 min after NEB, Fig. 3*C*). In contrast, centromeres in Rod$^{\Delta/\Delta}$ cells display no predominant direction during this stage of spindle assembly. At later times (>3 min after NEB), centromere movements become more organized, but their magnitude is consistently lower than in RPE1 cells (Fig. 3*C*). Thus, activities associated with the kinetochore corona determine directionality, timing, and the magnitude of centromere movements during early prometaphase.

Centromere Velocity Varies with the Distance to the Spindle Center, and It Depends on the Presence of the Kinetochore Corona. To gain insight into the nature of forces that position chromosomes during prometaphase, we compare velocities of centromere movements at various times and in various parts of the spindle. In RPE1 cells, the mean speed of centromeres peaks at 2.0 ± 1.4 μm/min at 60 to 90 s after NEB and subsequently decreases to 1.5 ± 1.0 μm/min (Fig. 4*A*). In Rod$^{\Delta/\Delta}$ cells, the mean speed remains constant throughout prometaphase at 1.4 ± 0.8 μm/min (Fig. 4*A*). These differences indicate that the lack of the kinetochore corona primarily affects movements of centromeres during the early stages of spindle assembly, prior to the formation of amphitelic attachments. To test this possibility, we split centromere trajectories into two periods: "preamphitelic" and "amphitelic." The time of amphitelic attachment formation is detected using the previously established criteria (9). This decomposition allows us to isolate the initial large-scale congression phase (preamphitelic), which is the focus of this study, from the final establishment of biorientation (amphitelic) that occurs within the spatial domain enriched with microtubule bundles characterized previously (9). We find that most preamphitelic movements are slow at a 1.2 μm/min median speed; however, rapid movements up to 19.7 μm/min are also observed in RPE1 (Fig. 4*B*). Rod$^{\Delta/\Delta}$ cells display the same median speed but lack rapid movements (Fig. 4*B*, maximum observed speed = 7.4 μm/min). Thus, preamphitelic kinetochores that lack the corona lose the ability to move at higher speed. For the centromeres that have established amphitelic attachments, the median speed is slightly lower in Rod$^{\Delta/\Delta}$ cells (Fig. 4*C*). As expected, rapid movements (>7.5 μm/min) are not observed among the amphitelic centromeres in either cell type (Fig. 4*C*).

Cytoplasmic dynein at the kinetochore corona has been implicated in rapid (up to 50 μm/min) movement of centromeres (20, 21). These movements, triggered by the initial contact between a kinetochore that lacks end-on-attached MTs and an astral MT (5, 20–22) are not expected in Rod$^{\Delta/\Delta}$ cells. Consistent with this notion, we find that the maximum speed achieved by a typical centromere in Rod$^{\Delta/\Delta}$ is less than 4 μm/min and this maximum is equally likely to be achieved at any stage of prometaphase (Fig. 4*D*). In contrast, centromeres achieve their maximum speed during early prometaphase in RPE1 (Fig. 4*E*). At this stage, ~7.5% centromeres briefly (<15 s) exceed 8 μm/min velocity; however, most centromeres never move faster than 5 μm/min (Fig. 4*E*). Thus, dynein-mediated gliding of unattached kinetochores alongside astral MTs occurs infrequently.

The wide range of speeds displayed by preamphitelic centromeres in RPE1 prompted us to compare movements of centromeres in various parts of the spindle. In RPE1 cells, the mean speed of centromeres at the periphery (>4 μm from the spindle center) is twofold greater than near the spindle center. In contrast, centromere mean speed is similar throughout the spindle in Rod$^{\Delta/\Delta}$ cells (Fig. 4*F*). We also separately assess the axial (Z displacement over time) and equatorial (ρ displacement over time) components of centromere movements. For the axial component, direction toward one pole is considered as positive and toward the opposite pole as negative. We find that the mean axial velocity is near zero at all distances from the spindle center in both RPE1 and Rod$^{\Delta/\Delta}$ cells (Fig. 4*G*), which suggests that centromeres display balanced fluctuations along the spindle axis with no preference for a particular pole. In contrast, mean equatorial velocity (positive toward the spindle axis and negative away from the axis) is nearly zero near the spindle center (<4 μm), it progressively increases at larger distances (4 to 7 μm), and is constant at distances >7 μm from the spindle center (Fig. 4*H*). In Rod$^{\Delta/\Delta}$ cells,

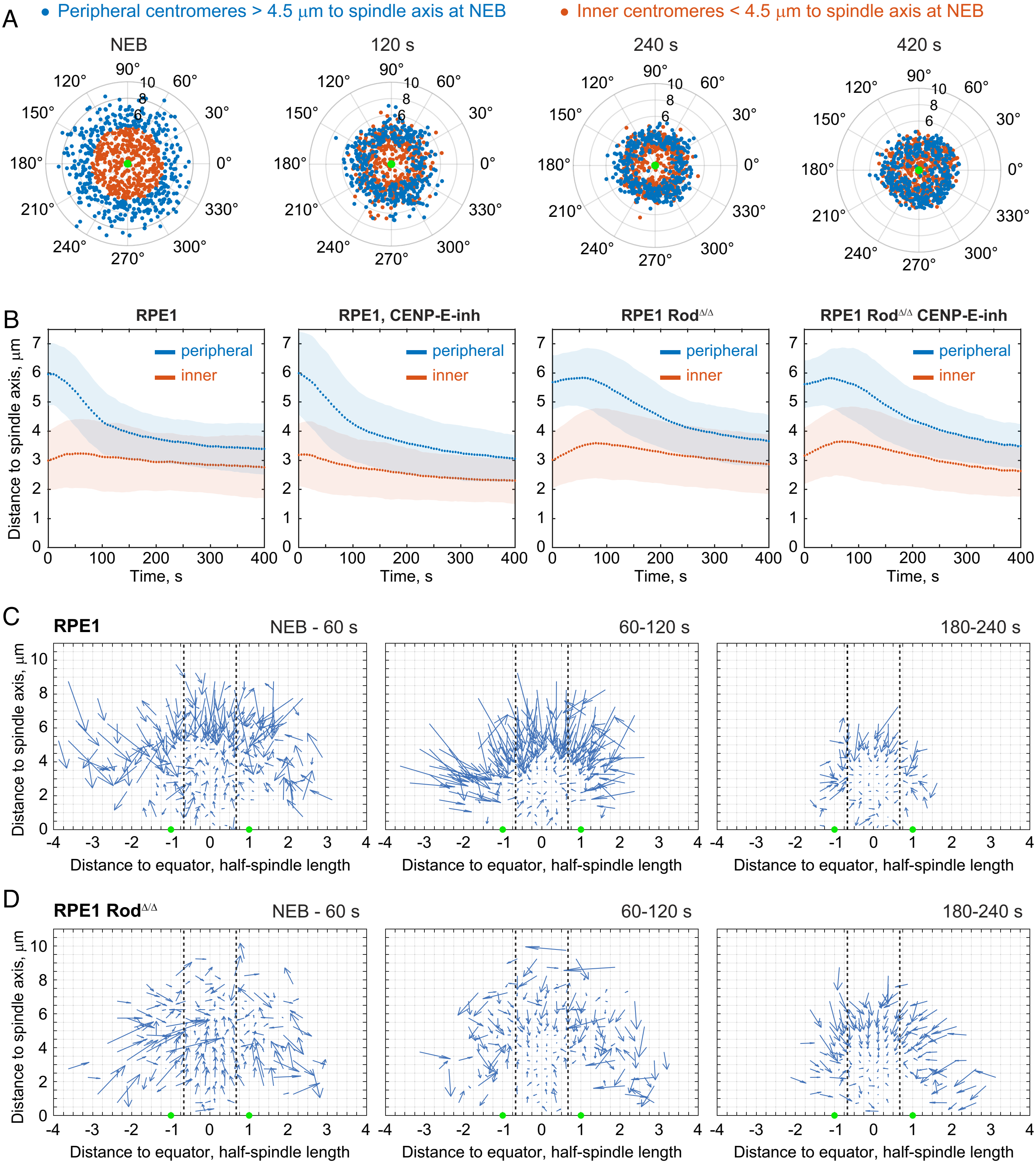

Fig. 3. Kinetochore corona facilitates rapid convergence of the peripheral centromeres toward the spindle center. (*A*) Radial-angular ρ-θ distribution of centromeres during prometaphase in RPE1 cells (876 centromeres in 19 cells). Peripheral centromeres (blue) rapidly (<240 s) gather into a ring around the spindle axis. (*B*) Mean (with SD) distance from the spindle axis to the "peripheral" (blue) and "inner" (orange) centromeres during prometaphase. CENP-E activity is inhibited with 20-nM GSK923295 (CENP-E-inh). (*C*, *D*) Quiver plots showing the direction and amplitude of centromere movements. Each arrow depicts the mean position change for all chromosomes within a small spatial bin over the specified time interval. Dashed black lines mark monoorientation zones of the spindle. RPE1 cells (*C*) display prominent near-synchronous centripetal movements, which are absent in Rod$^{\Delta/\Delta}$ cells (*D*).

the sigmoid dependency of equatorial velocity on the distance to the spindle center is qualitatively similar but significantly less pronounced (Fig. 4*H*). These observations suggest that the magnitude of the force moving centromeres toward the spindle axis changes in a nonlinear fashion, and this force is weaker in Rod$^{\Delta/\Delta}$ cells.

The observed dependency of the equatorial velocity of centromeres may arise from the increased resistance due to gradual crowding within the inner parts of the spindle. We test this possibility with two approaches. First, we compare velocity distributions between two populations of centromeres: those residing

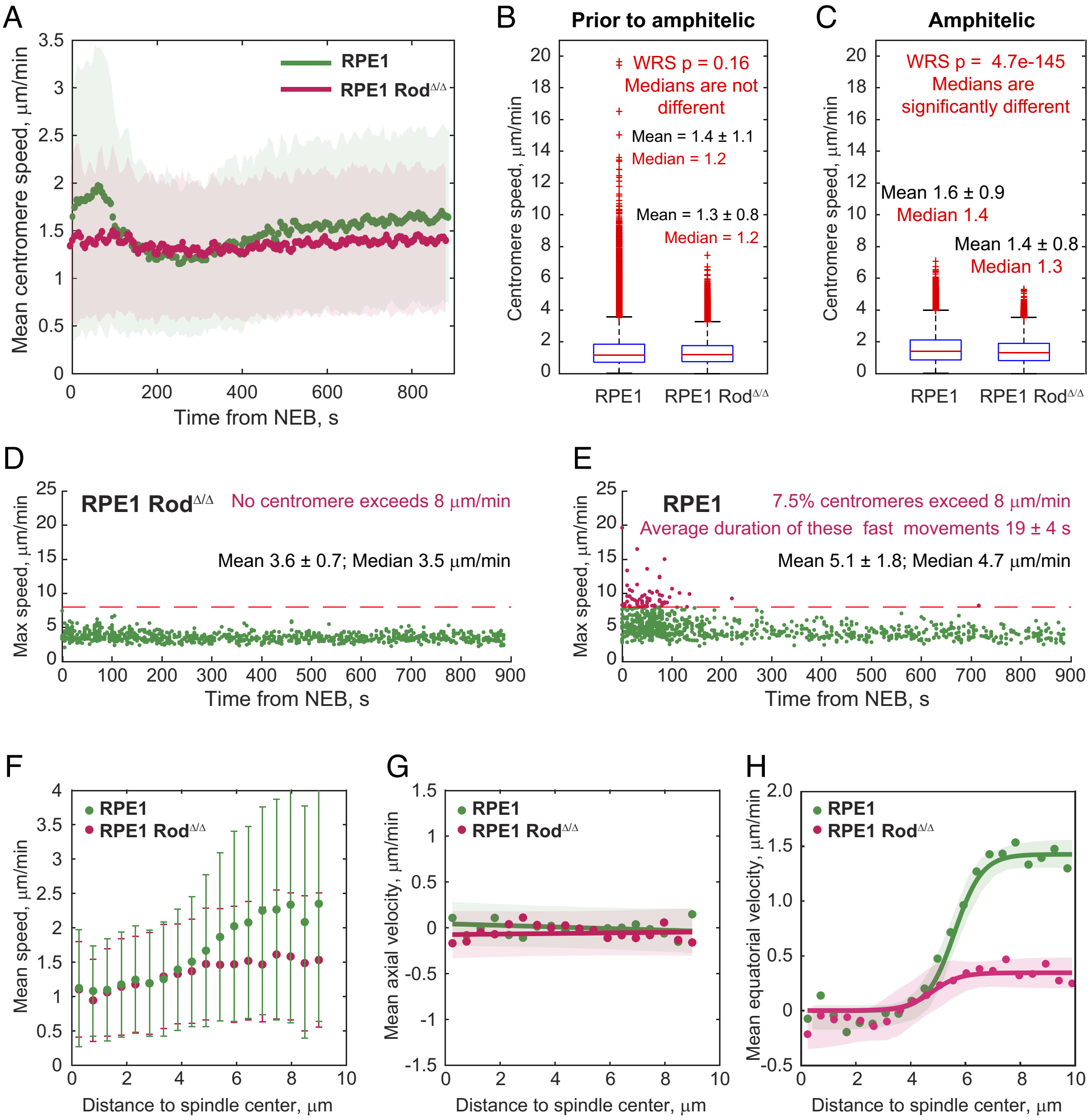

Fig. 4. Centromere velocities in RPE1 vs. Rod$^{\Delta/\Delta}$ cells at various stages of spindle assembly and in various parts of the cell. (*A*) Mean ± SD speed of centromere movements during prometaphase in RPE1 vs. RPE1 Rod$^{\Delta/\Delta}$ cells. In RPE1 cells, mean centromere speed is greater in the first 60 to 90 s after NEB, whereas in Rod$^{\Delta/\Delta}$ cells the mean velocity is constant throughout prometaphase. (*B* and *C*) Distribution of centromere instantaneous speed (position change over 15 s period) prior to (*B*), and after (*C*) formation of amphitelic attachment in RPE1 and Rod$^{\Delta/\Delta}$ cells. Median values are compared in the Wilcoxon Rank Sum (WRS) test. (*D* and *E*) Maximum speed achieved by each centromere during prometaphase in Rod$^{\Delta/\Delta}$ (*D*) and RPE1 (*E*) cells. Extremely rapid movements (>8 μm/min) are rare during early prometaphase in RPE1 cells and absent in Rod$^{\Delta/\Delta}$. (*F*) Mean centromere velocity as a function of distance to the spindle center in RPE1 vs. RPE1 Rod$^{\Delta/\Delta}$ cells. Error bars are SD. Notice that in RPE1 cells, centromeres move significantly faster in the periphery (>4 μm from the spindle center (*G* and *H*) Axial (*G*) and equatorial (*H*) components of centromere velocity as a function of distance to the spindle center. For the axial component (Z displacement over time), movement toward one pole is assigned a positive value and toward the opposite pole is negative. For the equatorial component (ρ displacement over time) movements toward the spindle axis are positive and away are negative. Lines represent linear (*G*) or logistic (*H*) functions fit to all velocity measurements (excluding large jumps, >8 μm/min), binned by the centromere's current position. Shaded corridors are 95% CI for the fits. In (*G*), near-zero mean velocities at all distances indicate no axial bias; in (*H*), positive values at larger distances reveal directional bias toward the spindle axis.

closer to the spindle center vs. those that are >5 μm away from the center at NEB. By virtue of their initial positioning, the former move within the central part of the spindle earlier, while the latter reach the inner parts of the spindle later when the crowding is already significant. We find that both groups exhibit similar velocities at 3 to 5 μm distances from the spindle center (*SI Appendix*, Fig. S4*A*). In contrast, within the group of initially peripheral centromeres velocities differ significantly at larger and smaller distances to the spindle center (*SI Appendix*, Fig. S4*B*). This analysis supports the notion that the velocity is distance- but not time-dependent, i.e., the slower movement near the spindle center is not due to the gradual crowding of the space by the arriving chromosomes. Second, we test whether the dependency of the equatorial velocity on the distance is affected by inactivation of the "spindle ejection force" mediated by chromokinesins KID (kinesin-10) and Kif4A (kinesin-4) (23). Simultaneous depletion of both motors via siRNA in RPE1 prevents the exclusion of chromosomes from the central part of the spindle during prometaphase (*SI Appendix*, Fig. S4*C*). Further, chromosome arms that normally orient in a radial array with their telomeres pointing outward from the spindle axis, become disorganized (*SI Appendix*, Fig. S4*D*). This change in the spindle architecture increases crowding of the inner spindle regions. Yet, no significant changes are observed in the mean centromere speed or the axial and equatorial velocities at various distances from the spindle center (*SI Appendix*, Fig. S4 *E*–*G*).

MTs Appear at Kinetochores Concurrently with the Initiation of NEB. In mammalian cells, forces for centromere movement have been shown to apply at two locales: at the kinetochore and at the distal ends of MTs attached to the kinetochore (7, 24). Considering recent observations that MT nucleation at the kinetochore corona is required for efficient chromosome congression (16), it is possible that the latter mechanism contributes significantly to spindle assembly. This possibility is supported by the demonstration that kinetochore attachment to short noncentrosomal MTs is common during prometaphase in RPE1 cells (8). Whether kinetochores attach to short MTs early enough to play a role in the initial congression is not known. We assess when kinetochores begin to interact with MTs by correlative light/electron microscopy (CLEM) of cells during the process of NEB.

Live-cell recording of RPE1 cells (55 recordings) with labeled chromosomes and nuclear envelope demonstrates that disassembly of the nuclear envelope consistently initiates near the equatorial plane of the nucleus. Multiple small fenestrae appear in a seemingly random pattern around the nuclear perimeter. The number and size of these fenestrae increase and ~3 min later only remnants of the nuclear envelope are seen around the central part of the forming spindle (Fig. 5*A*). Concurrently with fenestration of nuclear envelope, chromosomes adjacent to the fenestra initiate directional movements. At this time, kinetochores positioned deeper inside the nucleus are still shielded by the remnants of the nuclear envelope (Fig. 5*A*).

Guided by the time course of NEB visualized in the live-cell recordings, we fixed six RPE1 cells with GFP-labeled kinetochores and centrioles at the earliest signs of NEB. In three of these cells, the nuclear envelope was completely intact, and no MT was detected within the nuclear volume. In the other three cells, several fenestrae of various sizes are present in the nuclear envelope (*SI Appendix*, Fig. S5*A*). Consistent with the live-cell recordings, these fenestrae are near the equatorial plane of the forming spindle. The centrosomes reside within deep invaginations of the nuclear envelope on the ventral and dorsal sides of the nucleus (Fig. 5*B* and *SI Appendix*, Fig. S5*A*). Unexpectedly, we find MTs associated with some kinetochores irrespective of whether these kinetochores are near a fenestra or deep inside the nucleus (Fig. 5 *B* and *B′*). Both end-on attached and laterally interacting MTs are present (Fig. 5*C* and *SI Appendix*, Fig. S5*B*). The number of centromeres with MTs attached to at least one of the sister kinetochores varies among the three reconstructed cells (32 of 47; 23 of 46; and 1 of 46) and this number is larger in cells with larger fenestrae. In the earliest cell that contained just two small fenestrae, the only centromere associated with MTs is adjacent to a fenestra (*SI Appendix*, Fig. S5 *C* and *D*). Thus, noncentrosomal MTs begin to appear at kinetochores concurrently with the initiation of nuclear envelope fenestration and the number of kinetochores attached to short

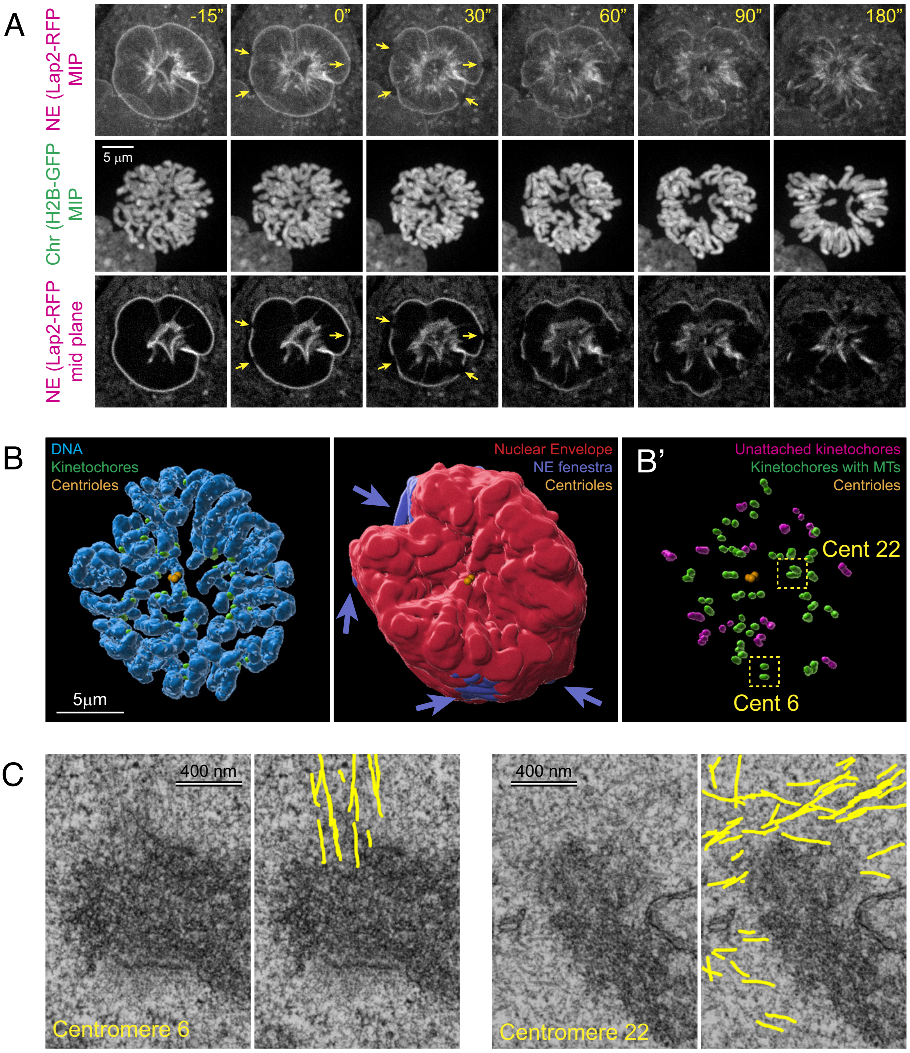

Fig. 5. Noncentrosomal microtubules appear at kinetochores concurrently with the breakdown of nuclear envelope. (*A*) Nuclear envelope (NE) is labeled via Lap2b-RFP and chromosomes (Chr)—via H2B-GFP. Upper rows show maximum-intensity projections (MIP) of the entire cell. The bottom row depicts a single focal plane in the middle of the cell. Arrows point at the fenestrae that initiate NE breakdown. Time is in seconds from the formation of the first fenestra. (*B*) Correlative LM/EM reconstruction of chromosomes (blue), centrioles (orange), kinetochores (green), and NE (red) in an RPE1 fixed during NEB. Arrows point at fenestrae in the NE. Fenestrae are distant and not in direct line of sight from the spindle poles (centrioles). (*B′*) Positions of centromeres with (green) or without (magenta) MTs in the immediate proximity of at least one of the sister kinetochores. (*C*) Examples of microtubule attachment to kinetochores positioned near a fenestra (Centromere 6, boxed in *B′*) or deep inside the nucleus (Centromere 22, boxed in *B′*). Notice both end-on and lateral interactions between the kinetochores and MTs.

noncentrosomal MTs increases rapidly during NEB (prior to the initiation of centromere movements).

Mechanistic Model for the Early Chromosome Congression Via Dynamic Interactions between the Spindle and MTs at the Kinetochore. Our analyses of centromere behavior reveal two prominent features of the early-prometaphase chromosome congression: 1) Centromeres move predominantly inward toward the spindle center rather than toward a spindle pole; 2) Mean velocity of the inward centromere movement is constant far from the spindle center, decreases at intermediate distances (between 7 and 4 µm), and the inward movement ceases when centromeres are closer to the center. Further, we find that many, potentially most, kinetochores are already attached to skMTs when they encounter MTs of the spindle proper. Thus, the force that moves the centromere can act on the kinetochore or at the distal ends of skMTs. These findings prompt an exploration of various kinetochore–MT interactions that explain the observed centromere behavior.

Our observations that centromeres move roughly orthogonal to the spindle axis suggest that the movement is driven by a balanced interaction with MTs that emanate from both spindle poles. For the centromere to move toward the spindle axis (inward), these forces must be directed toward the minus ends of spindle MTs. Consistent with this expectation, parameters of the initial congression are largely not affected by the inhibition of CENP-E, the only plus-end directed motor at the kinetochore (Figs. 2*B* and 3*B*).

To evaluate the character of MT interactions capable of gathering the scattered centromeres near the equator with the dynamics observed in RPE1 cells we construct a series of computational models (*SI Appendix*, *Supporting Text*). In the first model, kinetochores form stable (infinite-duration) connections to the walls of MTs produced by the spindle poles. This model stems from the observations of dynein-mediated lateral gliding of kinetochores along astral MTs (20, 21). Simultaneous interactions with MTs from the opposite spindle poles yield constant forces directed toward the minus ends of connected MTs which effectively "reels in" the attached MTs (Fig. 6*A*). As a result, centromeres would move toward the spindle axis (Fig. 6*A*′) akin to lifting an object by pulling on two ropes fixed at two points on the ceiling. An essential condition in this model is the ability of MTs to pivot at

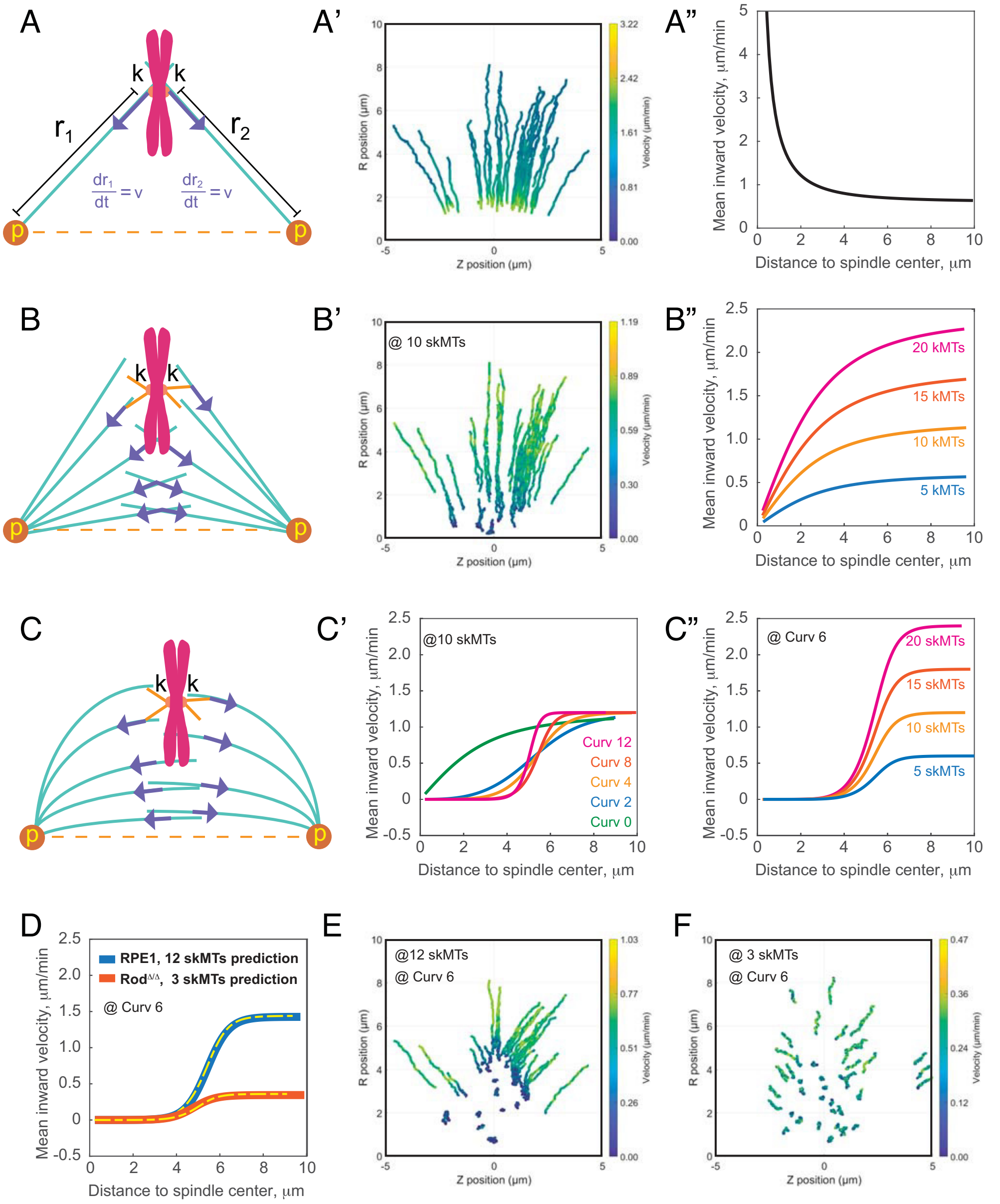

Fig. 6. Mechanistic models for early prometaphase chromosome congression. (*A*–*A*″) Stable interactions with spindle microtubules. (*A*) Kinetochores (k) form stable connections with long MTs (green) originating from the spindle poles (p). The force produced by the interaction with a single MT at the kinetochore plate (purple arrows) is directed toward the minus end of the MT residing at the spindle pole. Interaction with multiple MTs originating from both spindle poles moves the centromere inward. (*A*′) Early-prometaphase (0 to 4 min) centromere trajectories predicted by the model. (*A*″) Predicted mean centromere inward velocity at various distances from the spindle center. (*B*–*B*″) Transient interactions with straight spindle microtubules. (*B*) Minus end-directed forces are generated at the distal ends of short MTs protruding from kinetochores (skMTs, orange lines). Each interaction produces a force directed toward the minus end of the spindle MT. Individual encounters between MTs are brief (seconds) but multiple MTs protrude from each kinetochore, and interact with different MTs within the spindle. (*B*′) Early-prometaphase centromere trajectories predicted by the model. (*B*″) Predicted mean centromere inward velocity at various distances from the spindle center for various skMTs numbers. (*C*–*C*″) Transient interactions with curved spindle microtubules. (*C*) As in (*B*) but MTs are curved to mimic spindle geometry. (*C*′) Effects of MT curvature on the mean centromere inward velocity at various distances from the spindle center (at constant skMT number). (*C*″) Effects of skMT numbers on the mean centromere inward velocity at various distances from the spindle center (at constant spindle MT curvature). (*D*) Mean centromere inward velocity at various distances from the spindle center observed (solid lines) in cells and predicted (dashed lines) by the model outlined in (*C*). (*E* and *F*) Early-prometaphase centromere trajectories predicted for kinetochores with 12 (*E*) or 3 (*F*) skMTs by the model outlined in (*C*). All other parameters of the model are constant.

the centrosome into an antiparallel configuration (25–27). However, the inward centromere velocity is predicted to be lower at larger distances from the spindle center, as the angle between the opposed MTs changes at a lower rate closer to the axis (Fig. 6*A″* and *SI Appendix, Supporting Text*). The change in the angle between the vectors of the opposing forces translates the constant reeling-in rate in the periphery of the spindle into a faster movement near the spindle axis. Thus, centromere behavior observed in cells during early prometaphase cannot be explained by stable interactions between sister kinetochores and MTs from the opposite spindle poles.

As an alternative, we considered live-cell observations of transient dynein-mediated interactions at the distal ends of skMTs and spindle MTs (7, 8, 24). Chromosomes propelled by these interactions exhibit characteristic "jerks" rather than smoother linear movements (7, 8) which indicates that the force of constant magnitude is exerted randomly on a short timescale (seconds). In this scenario, congression is driven by numerous transient connections to multiple long MTs that are within the reach of skMTs (Fig. 6*B* and *SI Appendix, Supporting Text*). The transient-interaction model predicts that centromeres move predominantly inward, and their velocity is greater at larger distances from the spindle center (Fig. 6*B′*). Yet quantitatively the velocity–distance function predicted by the model differs significantly from the sigmoid dependency observed in cells (Fig. 6*B″*).

Our previous findings that the shape and architecture of the spindle determine the time and place of amphitelic attachment formation (9) inspired us to explore the transient-interaction model in the context of a more realistic geometry of spindle MTs. Chromosome congression has been shown to be less efficient in cells that lack the MT crosslinker PRC1 (9, 28). We reasoned that without the cross-links, MTs are less likely to bend toward the equator and tend to grow in more normal directions to the spindle axis. Analyses of centromere movements in PRC1-depleted cells reveal no significant changes in the total speed or mean velocity along the spindle axis (*SI Appendix*, Fig. S6 *A* and *B*). However, the dependency of the equatorial velocity on the distance to the center changes significantly: the inward movement is slower at intermediate distances but at larger distances from the spindle center the velocity is significantly higher than in untreated RPE1 cells (*SI Appendix*, Fig. S6*C*). These effects support the notion that the shape of spindle MTs must be considered in modeling of chromosome behavior.

The modified transient-interaction model with MTs curved along ellipsoidal surfaces that resemble the shape of prometaphase spindle (Fig. 6*C* and *SI Appendix, Supporting Text*) correctly predicts a sigmoid dependency of the inward velocity on the distance to the spindle center. The exact shape and magnitude of the predicted function depend on multiple parameters (*SI Appendix, Model Details and Derivations*) with the curvature of spindle MTs (Fig. 6*C′*) and the number of short MTs protruding from the kinetochores (Fig. 6*C″*) being particularly important. Guided by our recent description of the spindle shape (9) and the numbers of MTs observed by EM at RPE1 kinetochores prior to amphitelic attachment formation (8) we find a combination of these parameters that predict the velocity–distance function that matches the one observed in RPE1 cells (Fig. 6*D*). At these parameters, the model predicts that the centromeres predominantly move toward the spindle center, but their inward movement ceases when they reach within 3-4 µm from the spindle axis (Fig. 6*E*). Further, the model predicts a steady decrease in the number of polar (inherently monooriented) chromosomes at 2.7 ± 0.9 per minute rate, which accurately matches our experimental observations (Fig. 2*B*, RPE1). Thus, the dynamics of congression for most chromosomes in RPE1 cells can be explained by transient (seconds) interactions between ~12 skMTs and antipolar arrays of properly shaped spindle MTs.

We then explore whether our computational model can explain the changes in the pattern and velocity of centromere movements observed in Rod$^{\Delta/\Delta}$ cells. Astoundingly, we find that decreasing the number of skMTs from 12 to 3 with no change in other parameters yields a predicted centromere velocity–distance function that perfectly matches the experimental function observed in Rod$^{\Delta/\Delta}$ cells (Fig. 6*D*). Further, predicted trajectories (Fig. 6*F*) are consistent with the lack of directionality in centromere movements observed in Rod$^{\Delta/\Delta}$ (Fig. 3*D*). Furthermore, the rate of monoorientation correction is predicted to be 1.5 ± 0.6 chr/min, which matches the experimentally observed (Fig. 2*B*, Rod$^{\Delta/\Delta}$). Thus, the numerous abnormalities observed in cells lacking the RZZ complex can be explained solely by the lower number of skMTs due to the lower efficiency of MT nucleation at the kinetochores (16, 18).

Discussion

Inefficient chromosome congression, manifested by the increased number and persistence of monooriented chromosomes, is perhaps the most common abnormality of cell division (12). Numerous molecular deficiencies have been linked to hindered congression; however, mechanistic understanding of how the initially scattered chromosomes rapidly converge in a tight plate near the equator is lacking (12, 29). A key impediment has been the lack of quantitative characterization of chromosome behavior during early spindle assembly. Here we use an unbiased population-level analysis of centromere movements in various parts of the spindle. Three characteristic features of early-prometaphase chromosome behavior emerge from these analyses: 1) Centromeres initiate directional movements concurrently with the NEB; 2) Scattered centromeres predominantly move directly toward the center of the spindle and rarely toward a spindle pole. Indeed, the number of monooriented chromosomes is maximal at NEB; 3) Velocity of the centripetal centromere movement decreases as the centromere approaches the spindle axis. These features are not consistent with the chromosome behavior envisioned in the current models of spindle assembly that stem from the "Search and Capture" hypothesis (30).

It is commonly assumed that prior to their attachments to MT plus ends, kinetochores glide alongside MTs via forces generated by MT motors within the kinetochore's outer plate. CENP-E-dependent movements along MT bundles toward the plus ends as well as remarkably rapid dynein-dependent minus-end directed gliding along single MTs have been directly observed in cells (20, 21, 29, 31). Consistent with the latter observations, we also detect rapid (>8 µm/min) kinetochore movements in the wild-type RPE1 but not in Rod$^{\Delta/\Delta}$ cells that lack dynein at their kinetochores (Fig. 4 *B* and *C*). However, these rapid dynein-dependent movements are infrequent (7 to 8% of chromosomes) and thus they are unlikely to make a major contribution to the initial congression.

Strong evidence exists that dynein and CENP-E preferentially engage tyrosinated and detyrosinated MTs respectively and the difference in posttranslational modifications of more stable vs. more dynamic microtubules control directionality of kinetochore movements (32, 33). As during the early stages of spindle assembly, essentially all microtubules are tyrosinated, predominantly dynein activity at kinetochores is expected to move them toward a spindle pole. Monoorientation, created by this early dynein activity, is subsequently corrected by the CENP-E-mediated movement to the plus ends of MTs near the spindle equator (32). In this scenario, lack of dynein at the kinetochore should suppress monoorientation, while lack of CENP-E activity should impede congression of monooriented chromosomes (12, 34). Yet, our systematic analyses of centromere movement during early prometaphase demonstrate that inhibition of CENP-E does not impede relocation of centromeres closer to the center of the spindle (Figs. 2 and 3, CENP-E-inh). In contrast, chromosome movements toward the spindle center are impeded in cells that lack dynein at the kinetochores (Figs. 2 and 3, Rod$^{\Delta/\Delta}$). These effects are the opposite of that expected for centromere movements driven by motors residing within the kinetochore and asynchronous capture of astral MT by sister kinetochores. While other theoretical models propose that length-dependent forces on established, end-on attached K-fibers contribute to congression (35), our findings indicate the initial gathering of chromosomes is a distinct, earlier process. Thus, while some chromosomes clearly follow the classic monoorientation–congression pattern during prometaphase, this behavior is not common.

Two intriguing features of centromere movements during early prometaphase are the predominant centripetal direction of the movement and the sigmoid dependency of centromere velocity on the distance from the center. We test several models that could explain these features and arrive at a single plausible mechanism. Common in all tested models is that a centromere with two sister kinetochores engages MTs from both spindle poles. This feature is necessary to explain the generally centripetal direction of the movement. However, a nearly synchronous capture of MTs from both spindle poles is possible only for unrealistically large kinetochores (36, 37). For example, if ~1,000 MTs splay out from each centrosome and the nuclear volume is roughly a cylinder with 4 μm height 10 μm radius, then, at the cylindrical surface farthest away from the spindle center, a single MT contact requires no less than 0.5 × 0.5 μm^2 area, which is significantly larger than the plate of a human kinetochore (38). The insufficient size problem would be resolved, if spindle MTs interact not with the kinetochore plate directly but with multiple short (<1 μm) pivoting MTs protruding from the plate.

Our live-cell and CLEM data suggest that laterally as well as end-on attached MTs begin to accumulate at kinetochores concurrently with the breakdown of nuclear envelope, prior to the initial contacts with spindle MTs (Fig. 5). These data are consistent with previous reports that the majority of RPE1 kinetochores (>75%) are in close contact with ~30 noncentrosomal MTs, >10 of which appear to attach end-on during mid-prometaphase (8). Thus, a typical kinetochore appears to bear multiple skMTs during its initial encounter with spindle MTs. A corollary of this feature is that spindle microtubules arriving near a centromere are more likely to interact with the protruding skMTs rather than with the kinetochore plate.

Distal ends of skMTs have been observed to rapidly connect to the walls of adjacent microtubules within the spindle and be pulled toward the minus ends of the spindle microtubules (7, 24) in a characteristic "jittery" pattern in which low-amplitude transient poleward jumps are intermittent with short pauses (7). In contrast, kinetochore gliding alongside astral MTs driven by dynein within the kinetochore outer layer is smooth (5, 22, 39). These observations support the idea that while the skMTs–MTs interaction produces a constant-magnitude net force, this force arises from the rapid attachment-detachment cycle exhibited by individual skMTs. Our computational analyses demonstrate that this type of interaction correctly explains centromere movements observed during early prometaphase (Fig. 6). Continuous gliding of kinetochores on intersections of astral MTs results in a wrong spatial distribution of centromere velocities and slower decrease in the number of monooriented chromosomes (Fig. 6 A′ and A″).

Formally, a gradual slowing down of centromeres' inward movements could be caused by a distance-dependent ejection force acting on the chromosome arms (40, 41) even in the case of stable interactions between kinetochores and astral MTs. However, the velocity–distance function does not change in cells depleted for both kinesin motors responsible for the ejection of chromosome arms (*SI Appendix*, Fig. S4*F*). Thus, the ejection force is not a major factor in the slower movement of centromeres near the spindle center. Nor do our analyses support the possibility that the slower movements in the inner parts of the spindle are due to crowding of the space by the arriving chromosomes (*SI Appendix*, Fig. S4 *A* and *B*). Ruling out these formal possibilities leaves the nature of interactions with spindle MTs as the only viable reason for the observed velocity–distance relationship.

While the prediction of the transient-interaction model that centromeres move slower near the spindle center holds for a wide range of MT distributions, matching the observed sigmoid velocity–distance dependency requires that MTs emanating from the spindle poles are curved along ellipsoidal surfaces that resemble the natural shape of the spindle (Fig. 6 *C* and *C*″). Remarkably, this modification of the model yields predicted distance-velocity functions that are indiscernible from the experimentally observed (Fig. 6*D*). Further, the prominent difference in the distance-velocity functions in RPE1 vs. Rod$^{\Delta/\Delta}$ arises from changing a single parameter of the model – the number of short MTs protruding from the kinetochore. Importantly, a lower number of short MTs at the kinetochore is expected as lack of dynein and more specifically its light intermediate chain at the kinetochore is known to suppress nucleation of MTs at the kinetochore corona (16).

Based on these observations, we propose that early-prometaphase behavior of chromosomes in human cells is principally determined by transient interactions between numerous short MTs protruding from the kinetochores and properly shaped and distributed spindle MTs (Fig. 7). These interactions, mediated by multivalent dynein complexes, result in rapid, short, and random, excursions of skMTs toward the minus ends of spindle MTs that radiate from both poles. Transient relatively weak interactions have been shown to be surprisingly impactful drivers of motion at the molecular scale in other contexts (42). Noteworthy is also that a single dynein motor is capable of generating forces that are an order of magnitude greater than the minimal force required for moving a chromosome (~0.1 pN, see ref. 43). An important advantage of brief contact in repeating detachment–reattachment cycles is that centromeres move toward the spindle center by making numerous contacts with various spindle MTs, rather than pulling along the same MTs all the time. Consequently, the direction and magnitude of the resultant force changes in different parts of the spindle. One potentially important function of the resulting telescopic velocity is to synchronize the arrival of centromeres to the area with high concentration of antiparallel bundles facilitating the efficient formation of amphitelic attachments (9).

The model we propose places directionality and density requirements on the MT network of the spindle. This sensitivity is highlighted by cells depleted of the MT crosslinker PRC1 (*SI Appendix*, Fig. S6), which exhibit a distinct velocity profile. While this altered profile is qualitatively consistent with a change in spindle geometry, quantitatively matching the data requires accounting for additional factors, such as a potential shift in the kinetic regime of MT interactions (*SI Appendix*, Supporting Text). Consistent with this complexity, it is now increasingly apparent that distinct populations of MTs in the spindle exist (44), and whether this intricate network of MTs (1) and KTs (45) in the prometaphase spindle corresponds to these requirements remains to be seen. Other interesting questions are how MT branching (46), viscoelastic nonlinear mechanics of MT network (47), and chromosome arms (48) could affect centromere convergence. Also, in other contexts, MT configurations can be optimized for cargo capture (49), and it would be interesting to investigate the optimal configurations of MTs for rapid

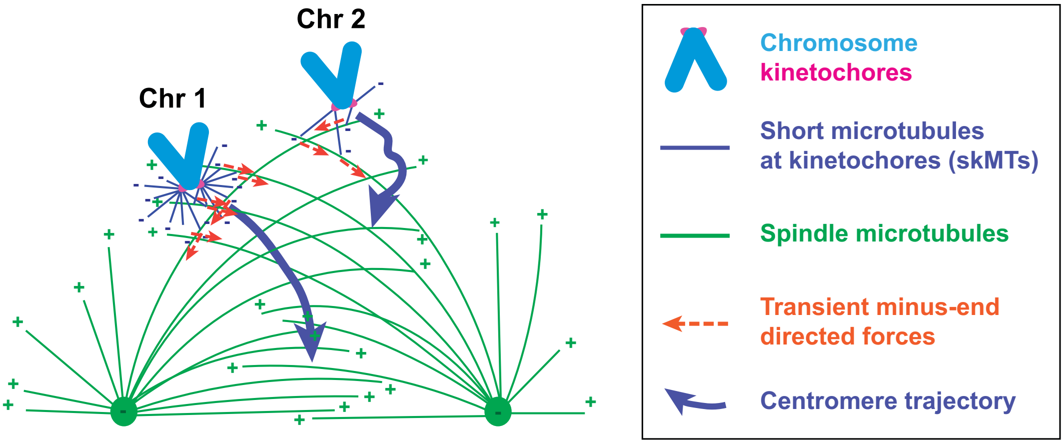

Fig. 7. Mechanism for centromere centripetal movements during early stages of spindle assembly. Gathering of the initially scattered chromosomes onto the equatorial plate during early prometaphase is driven primarily by transient interactions between skMTs protruding from kinetochores and curved MTs of the spindle ("Chr 1"). These interactions involve dynein that acts at the minus ends of skMTs. Magnitude of the resultant force and direction of centromere movement depends on the number of interactions (in turn determined by the number of skMTs) and the shape of spindle MTs. A sufficient number of skMTs in the context of properly shaped spindle MTs moves the centromere toward the spindle center (Chr1). The velocity decreases as the angle between the centromere trajectory and spindle MT changes. An insufficient number of skMTs, e.g., in cells with suppressed MT nucleation at the kinetochore (Rod$^{\Delta/\Delta}$) results in slower movement and loss of directionality ("Chr 2").

chromosome arrival to the spindle. Importantly, the model produces accurate quantitative predictions not just for the distance-velocity function but also for the rates of monoorientation correction.

Formally, in the presence of skMTs, direct interactions among these MTs could in principle drive chromosomes to converge on their center-of-mass and then pull the spindle poles into chromosome-defined positions (50), and similar arguments can be made for direct centromere–centromere interactions. However, we do not observe trajectory signatures consistent with such chromosome-driven mechanisms: early-prometaphase pole movements are insensitive to changes in centromere positions, and the centromere center-of-mass instead lags behind and follows the spindle center, whose position is determined by the centrosomes.

Another possibility that must formally be considered is that chromosomes initially gather closer to the spindle center via MT-independent mechanisms. Several studies suggest that contraction of actomyosin networks (51, 52), like a fishnet, can bring chromosomes closer to the spindle. This possibility is especially relevant because the telescopic inward velocity emerges naturally in the actomyosin networks (53). However, MT-independent mechanisms are inconsistent with the dramatic changes in centromere velocities and rate of monoorientation correction observed in Rod$^{\Delta/\Delta}$ cells. While these observations do not rule out involvement of actomyosin contractility in the initial congression, this mechanism is likely to be a relatively minor part of the early-prometaphase chromosome congression at most. Thus, the model described in Fig. 7 appears to offer the most reasonable mechanism of congression in human cells.

Materials and Methods

Cell Lines and Transfection. RPE1 cells coexpressing Centrin1-GFP and CenpA-GFP (13), RPE1 Rod$^{\Delta/\Delta}$ with the same markers (8, 9), RPE1 coexpressing H2B-Neon and mRFP-LAP2b (gift from D. Pellman, Dana Farber), RPE1 expressing Sh-PRC1, and RPE1 coexpressing Centrin1-YFP and CenpA-GFP (this study) were cultured in antibiotic-free DMEM/F-12 (Gibco) medium supplemented with 10% FBS (Gibco), at 37 °C, 5% CO$_2$. Culture media for RPE1 Rod$^{\Delta/\Delta}$ cells were additionally supplemented with 1 mM sodium pyruvate (Gibco). CENP-E was inhibited by 20 nM GSK-923295 (MedChemExpress) 0.5 to 2.5 h preimaging. To generate RPE1 cell line coexpressing Centrin1-YFP and CenpA-GFP, RPE1 cells were transfected with CenpA-GFP (LentiLox 3.1) lentivirus (with 1:100 Polybrene) for ~12 h as previously described (13): clones with strong CenpA-GFP labeling were isolated by limiting dilution, then transfected with Centrin1-YFP, with stable double-positive clones selected by microscopy. For depletion of chromokinesins, siRNA targeting Kid (5′-AAGCGCGCTTTGTAGGATTCG-3′) (41) and Kif4a (5′-CAGGTCCAGACTACTACTC-3′) (54) were cotransfected by electroporation (Nucleofector program X-001; Amaxa Biosystems) 48 h before imaging or fixation. Only cells displaying the phenotype (lacking chromosome ring in prometaphase) were analyzed. CENP-E depletion by siRNA transfection followed published protocols (8).

Live-Cell Microscopy. Cells were grown on #1.5 coverslips for 48 to 72 h. Media were replaced 24 h preimaging with phenol-red free DMEM/F-12 containing 10% FBS and Pen-Strep (P4333; Sigma). Coverslips were mounted in Rose chambers within a custom-built enclosure (37.0 ± 0.3 °C) ~3 h preimaging. Images were acquired on a Nikon Ti2E/Yokogawa X1 spinning-disk with a λPlanApo 100x1.45 NA oil objective. 488, 561, 640-nm excitation light intensities were kept at ~10 nW/mm^2. Recordings were collected every 5 s at 500 to 750 nm Z-steps (17 to 20 planes) and 110 nm XY pixel size; other recordings were performed at 15 to 30 s. Except for GSK-treated RPE1 Rod$^{\Delta/\Delta}$, datasets were reused from previous studies (8, 9). Images were processed using SoftWoRx 5.0 (Applied Precision) and Imaris (Oxford Instruments).

Immunofluorescence. Cells were pre-extracted (30 s) in warm PEM buffer (100 mM PIPES pH 7, 1 mM EDTA, 1 mM MgCl$_2$) with 0.5% Triton X-100 and fixed (10 min) in PEM with 3.2% paraformaldehyde (EM grade; EMS) and 0.1% glutaraldehyde (G5882; Sigma). After PBS washing, cells were reduced (5 min) with 30 mM sodium borohydride (452882; Sigma), and incubated (30 min) with blocking/permeabilization buffer (PBS, 3% BSA, 0.5% Triton X-100). Microtubules were visualized with DM1a anti-α-tubulin (1:200; Sigma T9026) followed by Alexa Fluor 647 secondary antibody (1:100; Invitrogen A21236); chromosomes were stained with 1 mg/mL Hoechst 33342 (Molecular Probes). Kid/Kif4A-depleted cells were lysed (1 min) in warm PEM buffer (pH 6.9, 2.5 mM EGTA, 5 mM MgCl$_2$) with 1% Triton X-100 before fixation in 1% glutaraldehyde. Images were acquired at 73 or 110-nm XY pixel size and 200-nm Z-steps, deconvolved (SoftWoRx 5.0; lens-specific PSF) and 3D-reconstructed (Imaris). Axial/equatorial views were aligned to spindle poles.

Correlative Light Electron Microscopy (CLEM). Cells were fixed (30 min) in 100 mM sodium cacodylate (pH 7.4; EMS) with 2.5% glutaraldehyde and stained for 5 min in 100 mM sodium cacodylate buffer with 1 mg/mL Hoechst 33342. Z-series were collected using the same acquisition parameters as fixed-cell immunofluorescence. After embedding/sectioning (55), 80-nm sections were imaged on a JEM 1400 microscope (JEOL; 80 kV) with side-mounted 4.0-megapixel XR401 sCMOS AMT camera. Whole-cell volumes were reconstructed from low-magnification (5 K) series and aligned to light microscopy using chromosome-arm positions; high-magnification (40 K) images resolved microtubule distribution.

Trajectory Processing. Instantaneous velocities, both experimental and simulation, were calculated by $\mathbf{v}(t) = [\mathbf{x}(t+\Delta t) - \mathbf{x}(t)]/\Delta t$ over $\Delta t = 15$ s (three frame intervals), with those >8 μm/min excluded as jumps. Velocity vectors were analyzed using two decompositions related to the spindle geometry: 1) cylindrical components derived from the pole–pole axis (radial v_r, axial v_z), or 2) projections relative to the spindle center. For the latter, a chromosome at position $\mathbf{x} = (z, r)$ with velocity $\mathbf{v}$ has a center-directed velocity defined by $v_{\text{center}} = \mathbf{v} \cdot \hat{\mathbf{u}}_{\text{center}}$ (where $\hat{\mathbf{u}}_{\text{center}} = -\mathbf{x}/\|\mathbf{x}\|$), and orthogonal velocity $v_{\text{ortho}} = \mathbf{v} \cdot \hat{\mathbf{u}}_{\perp}$ (where $\hat{\mathbf{u}}_{\perp}$ is a unit vector orthogonal to $\hat{\mathbf{u}}_{\text{center}}$). The filtered velocity data were grouped into equally spaced bins either by radial distance from the spindle axis (r) or by total distance from the spindle center ($d = \sqrt{z^2 + r^2}$). Distance-dependent mean velocities were fit with four-parameter logistic or two-parameter linear functions.

Computational Models and Simulation. We simulated two competing hypotheses in 2D cylindrical (z, r) coordinates with poles fixed at $(\pm L, 0)$, and $\Delta t_{sim} = 0.01$ s downsampled to $\Delta t = 5$ s to match experimental resolution. Initial chromosome positions were sampled from experimental distributions at NEB. The Stable Attachment model assumes chromosomes maintain persistent connections to microtubules from both poles, with motion driven by inward flux. The Transient Interaction model assumes motion arises from independent force-generating elements that stochastically cycle between binding (rate dependent on local microtubule density) and unbinding (constant probability) to a dense network. Force generators followed straight paths toward poles or curved paths defined by spindle geometry; regimes included microtubule-density-limited and motor-limited conditions. See *SI Appendix* for further details.

Data, Materials, and Software Availability. Tracking data, analysis code, and simulation software are available on Zenodo [https://doi.org/10.5281/zenodo.18167079, (56)].

ACKNOWLEDGMENTS. This work was supported by the NIH NIGMS grant GM130298 (A.K.), NSF Grants DMS 1953430 (A.M.) and CAREER DMS-2545859 (C.E.M.) and NSF/NIGMS Grant DMS-2451263 (C.E.M.).

Author affiliations: [a]Department of Mathematics, University of Utah, Salt Lake City, UT 84112; [b]Division of Genetics, Wadsworth Center, New York State Department of Health, Albany, NY 12237; [c]Department of Mathematics, New York University, New York, NY 10012; and [d]Department of Biology, New York University, New York, NY 10012

1. R. Kiewisz *et al.*, Three-dimensional structure of kinetochore-fibers in human mitotic spindles. *eLife* **11**, e75459 (2022).
2. E. O'Toole, M. Morphew, J. R. McIntosh, Electron tomography reveals aspects of spindle structure important for mechanical stability at metaphase. *Mol. Biol. Cell* **31**, 184–195 (2020).
3. S. Redemann *et al.*, *C. elegans* chromosomes connect to centrosomes by anchoring into the spindle network. *Nat. Commun.* **8**, 15288 (2017).
4. U. Euteneuer, J. R. McIntosh, Structural polarity of kinetochore microtubules in PtK1 cells. *J. Cell Biol.* **89**, 338–345 (1981).
5. J. H. Hayden, S. S. Bowser, C. L. Rieder, Kinetochores capture astral microtubules during chromosome attachment to the mitotic spindle: Direct visualization in live newt lung cells. *J. Cell Biol.* **111**, 1039–1045 (1990).
6. R. Heald, A. Khodjakov, Thirty years of search and capture: The complex simplicity of mitotic spindle assembly. *J. Cell Biol.* **211**, 1103–1111 (2015).
7. V. Sikirzhytski *et al.*, Direct kinetochore-spindle pole connections are not required for chromosome segregation. *J. Cell Biol.* **206**, 231–243 (2014).
8. V. Sikirzhytski *et al.*, Microtubules assemble near most kinetochores during early prometaphase in human cells. *J. Cell Biol.* **217**, 2647–2659 (2018).
9. F. Renda *et al.*, Non-centrosomal microtubules at kinetochores promote rapid chromosome biorientation during mitosis in human cells. *Curr. Biol.* **32**, 1049–1063.e1044 (2022).
10. K. M. Godek, L. Kabeche, D. A. Compton, Regulation of kinetochore-microtubule attachments through homeostatic control during mitosis. *Nat. Rev. Mol. Cell Biol.* **16**, 57–64 (2015).
11. K. Vukusic, I. M. Tolic, Polar chromosomes—Challenges of a risky path. *Cells* **11**, 1531 (2022).
12. H. Maiato, A. M. Gomes, F. Sousa, M. Barisic, Mechanisms of chromosome congression during mitosis. *Biology (Basel)* **6**, 13 (2017).
13. V. Magidson *et al.*, The spatial arrangement of chromosomes during prometaphase facilitates spindle assembly. *Cell* **146**, 555–567 (2011).
14. V. Nunes *et al.*, Centrosome-nuclear axis repositioning drives the assembly of a bipolar spindle scaffold to ensure mitotic fidelity. *Mol. Biol. Cell.* **31**, 1675–1690 (2020).
15. K. W. Wood *et al.*, Antitumor activity of an allosteric inhibitor of centromere-associated protein-E. *Proc. Natl. Acad. Sci. U.S.A.* **107**, 5839–5844 (2010).
16. J. Wu *et al.*, Microtubule nucleation from the fibrous corona by LIC1-pericentrin promotes chromosome congression. *Curr. Biol.* **33**, 912–925 (2023).
17. G. Kops, R. Gassmann, Crowning the kinetochore: The fibrous corona in chromosome segregation. *Trends Cell Biol.* **30**, 653–667 (2020).
18. Y. Ishikawa *et al.*, Fibrous corona is reduced in cancer cell lines that attenuate microtubule nucleation from kinetochores. *Cancer Sci.* **116**, 420–431 (2025).
19. J. A. Rodriguez-Rodriguez *et al.*, Distinct roles of RZZ and Bub1-KNL1 in mitotic checkpoint signaling and kinetochore expansion. *Curr. Biol.* **28**, 3422–3429.e3425 (2018).
20. Z. Yang, U. S. Tulu, P. Wadsworth, C. L. Rieder, Kinetochore dynein is required for chromosome motion and congression independent of the spindle checkpoint. *Curr. Biol.* **17**, 973–980 (2007).
21. C. L. Rieder, S. P. Alexander, Kinetochores are transported poleward along a single astral microtubule during chromosome attachment to the spindle in newt lung cells. *J. Cell Biol.* **110**, 81–95 (1990).
22. S. P. Alexander, C. L. Rieder, Chromosome motion during attachment to the vertebrate spindle: Initial saltatory-like behavior of chromosomes and quantitative analysis of force production by nascent kinetochore fibers. *J. Cell Biol.* **113**, 805–815 (1991).
23. C. Wandke *et al.*, Human chromokinesins promote chromosome congression and spindle microtubule dynamics during mitosis. *J. Cell Biol.* **198**, 847–863 (2012).
24. M. W. Elting, C. L. Hueschen, D. B. Udy, S. Dumont, Force on spindle microtubule minus ends moves chromosomes. *J. Cell Biol.* **206**, 245–256 (2014).
25. I. Kalinina *et al.*, Pivoting of microtubules around the spindle pole accelerates kinetochore capture. *Nat. Cell Biol.* **15**, 82–87 (2013).
26. C. Edelmaier *et al.*, Mechanisms of chromosome biorientation and bipolar spindle assembly analyzed by computational modeling. *eLife* **9**, e48787 (2020).
27. L. Winters *et al.*, Pivoting of microtubules driven by minus-end-directed motors leads to spindle assembly. *BMC Biol.* **17**, 42 (2019).
28. J. Matkovic *et al.*, Kinetochore- and chromosome-driven transition of microtubules into bundles promotes spindle assembly. *Nat. Commun.* **13**, 7307 (2022).
29. M. Barisic, P. Aguiar, S. Geley, H. Maiato, Kinetochore motors drive congression of peripheral polar chromosomes by overcoming random arm-ejection forces. *Nat. Cell Biol.* **16**, 1249–1256 (2014).
30. M. Kirschner, T. Mitchison, Beyond self-assembly: From microtubules to morphogenesis. *Cell* **45**, 329–342 (1986).
31. T. M. Kapoor *et al.*, Chromosomes can congress to the metaphase plate before biorientation. *Science* **311**, 388–391 (2006).
32. M. Barisic, H. Maiato, The tubulin code: A navigation system for chromosomes during mitosis. *Trends Cell Biol.* **26**, 766–775 (2016).
33. M. Barisic *et al.*, Microtubule detyrosination guides chromosomes during mitosis. *Science* **348**, 799–803 (2015).
34. F. Renda, A. Khodjakov, Role of spatial patterns and kinetochore architecture in spindle morphogenesis. *Semin. Cell Dev. Biol.* **117**, 75–85 (2021).
35. I. Sigmund, D. Božan, I. Šarić, N. Pavin, Mechanisms of chromosome positioning during mitosis. *PRX Life* **2**, 043017 (2024).
36. E. Kliuchnikov, A. Zhmurov, K. A. Marx, A. Mogilner, V. Barsegov, Cell DynaMo-stochastic reaction-diffusion-dynamics model: Application to search-and-capture process of mitotic spindle assembly. *PLoS Comput. Biol.* **18**, e1010165 (2022).
37. V. Magidson *et al.*, Adaptive changes in the kinetochore architecture facilitate proper spindle assembly. *Nat. Cell Biol.* **17**, 1134–1144 (2015).
38. F. Renda *et al.*, Effects of malleable kinetochore morphology on measurements of intrakinetochore tension. *Open Biol.* **10**, 200101 (2020).
39. R. V. Skibbens, C. L. Rieder, E. D. Salmon, Directional instability of kinetochore motility during chromosome congression and segregation in mitotic newt lung cells: A push-pull mechanism. *J. Cell Biol.* **122**, 859–875 (1993).
40. C. L. Rieder, E. D. Salmon, Motile kinetochores and polar ejection forces dictate chromosome position on the vertebrate mitotic spindle. *J. Cell Biol.* **124**, 223–233 (1994).
41. N. Tokai-Nishizumi, M. Ohsugi, E. Suzuki, T. Yamamoto, The chromokinesin Kid is required for maintenance of proper metaphase spindle size. *Mol. Biol. Cell* **16**, 5455–5463 (2005).
42. J. Newby *et al.*, A blueprint for robust crosslinking of mobile species in biogels with weakly adhesive molecular anchors. *Nat. Commun.* **8**, 833 (2017).
43. R. B. Nicklas, Chromosome velocity during mitosis as a function of chromosome size and position. *J. Cell Biol.* **25**, 119–135 (1965).
44. A. R. Tipton, G. J. Gorbsky, More than two populations of microtubules comprise the dynamic mitotic spindle. *J. Cell Sci.* **135**, jcs258745 (2022).
45. W. Conway *et al.*, Self-organization of kinetochore-fibers in human mitotic spindles. *eLife* **11**, e75458 (2022).
46. B. Gouveia *et al.*, Acentrosomal spindles assemble from branching microtubule nucleation near chromosomes in *Xenopus laevis* egg extract. *Nat. Commun.* **14**, 3696 (2023).
47. P. Suresh, V. Galstyan, R. Phillips, S. Dumont, Modeling and mechanical perturbations reveal how spatially regulated anchorage gives rise to spatially distinct mechanics across the mammalian spindle. *eLife* **11**, e79558 (2022).
48. A. E. C. Meijering *et al.*, Nonlinear mechanics of human mitotic chromosomes. *Nature* **605**, 545–550 (2022).
49. S. S. Mogre, J. R. Christensen, S. L. Reck-Peterson, E. F. Koslover, Optimizing microtubule arrangements for rapid cargo capture. *Biophys. J.* **120**, 4918–4931 (2021).
50. J. Mole-Bajer, The role of centrioles in the development of the astral spindle (newt). *Cytobios* **13**, 117–140 (1975).
51. P. Lenart *et al.*, A contractile nuclear actin network drives chromosome congression in oocytes. *Nature* **436**, 812–818 (2005).
52. A. J. Booth *et al.*, Contractile acto-myosin network on nuclear envelope remnants positions human chromosomes for mitosis. *eLife* **8**, e46902 (2019).
53. I. Linsmeier *et al.*, Disordered actomyosin networks are sufficient to produce cooperative and telescopic contractility. *Nat. Commun.* **7**, 12615 (2016).
54. E. Poser, R. Caous, U. Gruneberg, F. A. Barr, Aurora A promotes chromosome congression by activating the condensin-dependent pool of KIF4A. *J. Cell Biol.* **219**, e201905194 (2019).
55. C. L. Rieder, G. Cassels, Correlative light and electron microscopy of mitotic cells in monolayer cultures. *Methods Cell Biol.* **61**, 297–315 (1999).
56. C. Miles *et al.*, Data and Software for "The kinetochore corona orchestrates chromosome congression through transient microtubule interactions" (1.0.0). Zenodo. https://doi.org/10.5281/zenodo.18167079. Deposited 6 January 2026.

Supporting Information for

The kinetochore corona orchestrates chromosome congression through transient microtubule interactions

Christopher E. Miles[1*], Fioranna Renda[2*], Irina Tikhonenko[2], Angus Alfieri[2], Alex Mogilner[3], and Alexey Khodjakov[2]

Corresponding author: Christopher E. Miles

Email: chris.miles@utah.edu

This PDF file includes:

- Supporting text
- Figures S1 to S5
- Tables S1 to S3

Model Details and Derivations

S1. Introduction and Coordinate System

This supplement provides complete mathematical details for the chromosome movement models analyzed in the main text. We work in cylindrical coordinates (z, r) where z represents position along the spindle axis and r represents radial distance from this axis. The spindle poles are located at positions $\mathbf{p}_1 = (L, 0)$ and $\mathbf{p}_2 = (-L, 0)$, where L is the half-spindle length. Throughout this document, position vectors are denoted $\mathbf{x} = (z, r)$ and velocities as $\mathbf{v} = d\mathbf{x}/dt$. Time evolution follows the general form $d\mathbf{x}/dt = \mathbf{v}(\mathbf{x}, t) + \boldsymbol{\eta}(t)$ where $\boldsymbol{\eta}$ represents stochastic noise terms.

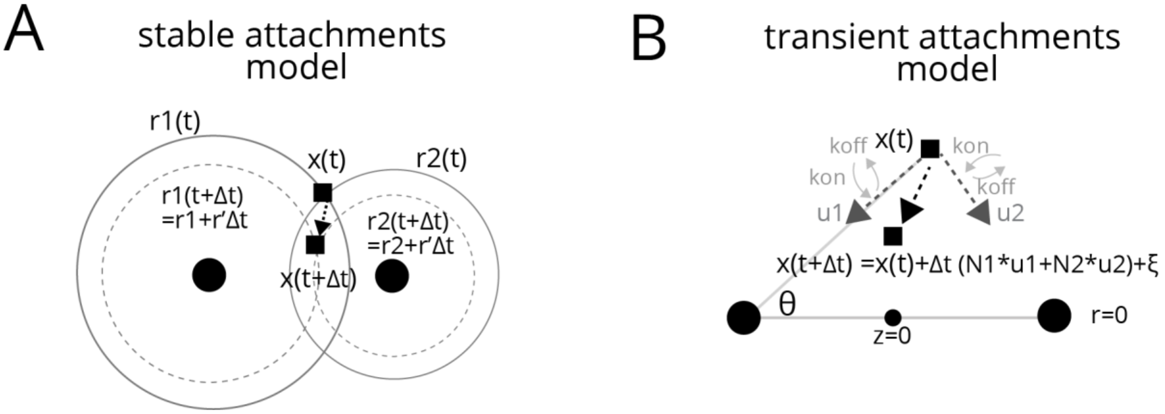

S2. Stable Attachment Model

S2.1 Biological Motivation and Assumptions

The stable attachment model represents the assumption that chromosome motion is driven by end-on attachments to microtubules emanating from opposite spindle poles. The key assumptions underlying this model are: (1) once attached, kinetochore-microtubule connections persist throughout prometaphase, (2) chromosomes remain tethered to both poles simultaneously, and (3) movement occurs through coordinated depolymerization of kinetochore microtubules, causing the effective "attachment spheres" centered at each pole to contract over time. This framework treats chromosome movement as purely geometric, determined by the intersection of two shrinking spheres.

S2.2 Mathematical Formulation

Consider a chromosome at position $\mathbf{x} = (z, r)$ connected to both spindle poles. The constraints imposed by stable attachments to the poles are:

$$\| \mathbf{x} - \mathbf{p}_1 \|^2 = r_1^2(t)$$
$$\| \mathbf{x} - \mathbf{p}_2 \|^2 = r_2^2(t)$$

where $r_1(t)$ and $r_2(t)$ are the time-dependent radii of the attachment spheres. Expanding these constraints:

$$r^2 + (z - L)^2 = r_1^2$$
$$r^2 + (z + L)^2 = r_2^2$$

The sphere radii evolve according to prescribed functions that can incorporate biological effects such as polar ejection forces:

$$\frac{dr_1}{dt} = v_r(r_1) + \sigma_1\sqrt{|v_r(r_1)|}\xi_1(t)$$
$$\frac{dr_2}{dt} = v_r(r_2) + \sigma_2\sqrt{|v_r(r_2)|}\xi_2(t)$$

where $v_r(r)$ represents the deterministic, distance-dependent rate of change of the sphere radius and $\xi_i(t)$ are independent white noise processes.

S2.3 Velocity Derivation

To find the chromosome velocity, we differentiate the constraint equations with respect to time:

$$\frac{d}{dt}[r^2 + (z-L)^2] = \frac{d}{dt}[r_1^2]$$
$$\frac{d}{dt}[r^2 + (z+L)^2] = \frac{d}{dt}[r_2^2]$$

Expanding the derivatives:

$$2r\frac{dr}{dt} + 2(z-L)\frac{dz}{dt} = 2r_1\frac{dr_1}{dt}$$
$$2r\frac{dr}{dt} + 2(z+L)\frac{dz}{dt} = 2r_2\frac{dr_2}{dt}$$

This linear system can be solved for the velocity components. Subtracting the first equation from the second:

$$2(z+L)\frac{dz}{dt} - 2(z-L)\frac{dz}{dt} = 2r_2\frac{dr_2}{dt} - 2r_1\frac{dr_1}{dt}$$
$$4L\frac{dz}{dt} = 2\left(r_2\frac{dr_2}{dt} - r_1\frac{dr_1}{dt}\right)$$

Therefore:

$$\frac{dz}{dt} = \frac{r_2\frac{dr_2}{dt} - r_1\frac{dr_1}{dt}}{2L}$$

Substituting back to find dr/dt, and after some algebra, we find

$$\frac{dr}{dt} = \frac{r_1\frac{dr_1}{dt}(z+L) - r_2\frac{dr_2}{dt}(z-L)}{2Lr}.$$

S2.4 Simulation Algorithm

The stable model simulation proceeds as follows:

1. Initialize chromosome positions from experimental data
2. Calculate initial sphere radii: $r_1 = \| \mathbf{x} - \mathbf{p}_1 \|$, $r_2 = \| \mathbf{x} - \mathbf{p}_2 \|$
3. At each timestep dt:
    - Update sphere radii: $r_i(t+dt) = r_i(t) + v_r(r_i)dt + \sigma_i\sqrt{|v_r(r_i)dt|}\eta_i$
    - Calculate new position using the velocity equations
    - Add Brownian noise: $\mathbf{x}(t+dt) = \mathbf{x}(t) + \mathbf{v}dt + \sigma\sqrt{dt}\boldsymbol{\eta}$

S2.5 Model Variants and Parameters

We examined two variants of the stable model:

Constant contraction: $v_r(r) = v_0$, a constant depolymerization rate.

Polar ejection forces: $v_r(r) = v_0\left(1 - \alpha\exp(-r/r_0)\right)$, captures the repulsive forces exerted by astral microtubules near the poles (causing expansion, $v_r > 0$) which slow sphere contraction when chromosomes are far from the poles.

S3. Transient Interaction Model

S3.1 Biological Motivation

The transient interaction model is motivated by the hypothesis that transient kinetochore-associated or short-microtubule-associated motors can transport chromosomes along the microtubules before stable end-on attachments form. Rather than maintaining persistent connections, chromosomes in this model undergo repeated cycles of binding to and unbinding from fixed-geometry microtubules throughout the spindle.

S3.2 Theoretical Foundation: Filament-Mediated Transport

To understand how transient interactions produce directed movement, we first derive the theoretical framework for transport in a filament network. Consider spindle poles at positions $(0, \pm L)$ that emit microtubules with a specified angular distribution. Each microtubule extends from its pole, and chromosomes can bind to these filaments and be transported toward the pole.

The key insight is that the local density of microtubules determines the binding probability, while the geometry of the filament network determines the direction of transport. We define the angular distribution $f(\theta)$ where θ is measured from the pole-to-pole axis. Specifically:

- For the pole at $z = +L$: $\theta = 0$ points toward $z = 0$ (downward along the spindle axis)
- For the pole at $z = -L$: $\theta = 0$ points toward $z = 0$ (upward along the spindle axis)
- For both poles: $\theta = \pi/2$ points perpendicular to the spindle axis

S3.3 Derivation of Microtubule Density

Starting from first principles, we calculate the spatial distribution of microtubules. Consider the upper pole at $z = +L$ emitting filaments. The probability of emitting a filament into solid angle $d\Omega$ in direction θ is: $dP = f(\theta)\sin(\theta)d\theta d\phi$, where the $\sin(\theta)$ factor accounts for the spherical coordinate measure. To find the density at position (z, r), we need to transform from spherical emission coordinates to cylindrical observation coordinates.

The transformation relationships are:

- Distance from pole: $R^2 = r^2 + (z - L)^2$

- Radial coordinate: $r = R\sin(\theta)$
- Axial coordinate: $z - L = -R\cos(\theta)$
- Angle: $\theta = \text{atan2}\big(r, -(z-L)\big)$

The Jacobian for the transformation from (R, θ) to (r, z) has determinant $|J| = 1/R$. Including the radial integration measure and transforming the probability element:

$$dP = f(\theta)\sin(\theta)d\theta d\phi dR = f(\theta)(r/R)(drdz/R)d\phi R = f(\theta)rdrdzd\phi$$

The density is defined such that the number of filaments in volume element $rdrdzd\phi$ is $\rho(r,z)rdrdzd\phi$. Therefore:

$$\rho_1(r,z) = \frac{f\Big(\text{atan2}\big(r, -(z-L)\big)\Big)}{r^2 + (z-L)^2}$$

By symmetry, the density from the lower pole is:

$$\rho_2(r,z) = \frac{f\big(\text{atan2}(r, z+L)\big)}{r^2 + (z+L)^2}.$$

S3.4 Transport Velocity in the Continuum Limit

When a chromosome binds to a microtubule, it moves toward the source pole with velocity directed along the filament. The unit vectors pointing from position (z, r) toward each pole are:

$$\hat{\mathbf{u}}_1 = \frac{(L-z, -r)}{\sqrt{(L-z)^2 + r^2}}$$

$$\hat{\mathbf{u}}_2 = \frac{(-L-z, -r)}{\sqrt{(-L-z)^2 + r^2}}$$

In the continuum limit, where binding and unbinding occur rapidly, the system reaches a steady state where the mean velocity is the sum of contributions from motors pulling toward each pole. This velocity is proportional to the number of engaged motors and the transport velocity per motor, and depends on the steady-state binding probabilities. The explicit form of this velocity is given by the mean-field approximation in section S4.2.

S3.5 Discrete Element Implementation

In the computational model, we implement this transport mechanism using discrete force-generating elements. Each chromosome has n independent elements (typically 10-20) that can be in one of three states:

- State -1: Bound to a microtubule from pole 1
- State 0: Unbound
- State +1: Bound to a microtubule from pole 2

The net velocity is the sum of contributions from all bound elements:

$$\mathbf{v} = \sum_i v_{\text{scale}}\, s_i \hat{\mathbf{u}}_{\text{pole}}(s_i)$$

where s_i is the state of element i and $\hat{\mathbf{u}}_{\text{pole}}$ points toward the appropriate pole.

S3.6 Binding Kinetics: Saturated and Unsaturated Regimes

The binding dynamics follow different kinetics depending on the experimental conditions:

Unsaturated Regime (General Case):
When motor proteins are limiting or microtubule density varies significantly, binding follows Michaelis-Menten kinetics:

$$P_{\text{bind},i} = k_{\text{on}} dt \left(\frac{\rho_i}{K_m + \rho_i}\right)$$

where K_m is the Michaelis constant representing the half-saturation density. This formulation captures the dependence on binding sites (spindle microtubules).

Saturated Regime (High Density Limit):
When microtubule density greatly exceeds K_m throughout the spindle ($\rho_i \gg K_m$), the Michaelis-Menten expression simplifies:

$$\lim_{\rho_i \gg K_m} \left(\frac{\rho_i}{K_m + \rho_i}\right) = 1$$

Therefore: $P_{\text{bind}} = k_{\text{on}} dt$ (independent of position)

This saturated regime represents control conditions where transient interactions are limited by motor kinetics rather than microtubule density. The steady-state probability of being bound to one pole when both are accessible is:

$$P_{\text{bound}} = \frac{k_{\text{on}}}{k_{\text{off}} + 2k_{\text{on}}}$$

S3.7 Force Direction: Straight vs. Curved Filaments

The direction of force depends on the geometry of microtubule trajectories. In the saturated limited, since the binding probability no longer depends on local density, we can formulate the model with other microtubule geometries.

Straight Filaments:
Forces point directly toward the poles along straight lines, using the unit vectors $\hat{\mathbf{u}}_1$ and $\hat{\mathbf{u}}_2$ defined earlier.

Curved Filaments:
Real spindle microtubules often follow curved paths. We model these using Lp-norm geometry:

$$\| \mathbf{x} \|_p = [|z|^p + |r/a|^p]^{1/p}$$

where $p = 2 +$ curvature (typically $p = 8$) and a is the aspect ratio. The force direction follows the gradient of this norm:
For pole 1: $\text{term}_1 = (L - z)^p + (r/a)^p$

$$v_{z,1} = -(L - z)^{p-1} \text{term}_1^{(1/p)-1}$$
$$v_{r,1} = -r^{-1} (r/a)^p \text{term}_1^{(1/p)-1}$$

These components are then normalized to obtain unit vectors. The velocity is set to zero on the spindle axis for the radial component, while preserving axial motion.

S3.8 Simulation Algorithm

The transient model simulation uses sub-timestep integration for accurate stochastic dynamics:

```
1.  Initialize positions and all elements to unbound state
2.  For each sub-timestep $dt_{\text{sub}} = 0.01s$:
    a. Calculate current position-dependent quantities (densities $\rho_i$ for unsaturated, force directions)
    b. For each force element:
        –   If bound: Check unbinding with $P_{\text{unbind}} = k_{\text{off}} dt_{\text{sub}}$
        –   If unbound: Check binding to each pole with appropriate probabilities
    c. Sum forces from all bound elements
    d. Update position: $\mathbf{x}(t + dt) = \mathbf{x}(t) + \mathbf{v}dt + \sigma\sqrt{dt}\boldsymbol{\eta}$
3.  Downsample to experimental time resolution
```

S4. Analytical Solutions

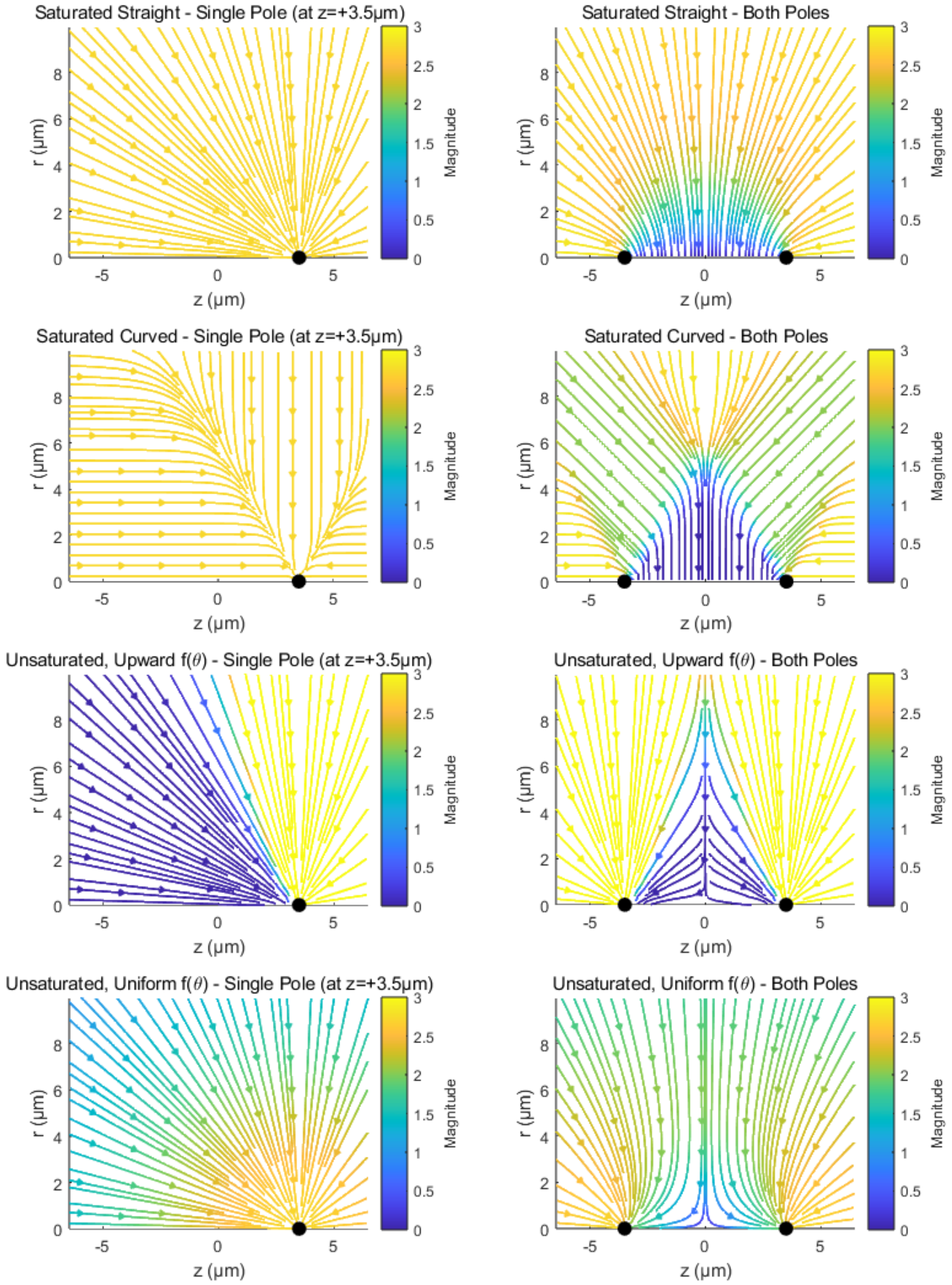

S4.1 Stable Model - Analytical Velocity

For the stable model at arbitrary position (z, r), the analytical velocities are:

$$\frac{dz}{dt} = \frac{r_2 v_r(r_2) - r_1 v_r(r_1)}{2L}$$

$$\frac{dr}{dt} = \frac{r_1 v_r(r_1)(z + L) - r_2 v_r(r_2)(z - L)}{2Lr}$$

where $r_1 = \sqrt{r^2 + (z - L)^2}$ and $r_2 = \sqrt{r^2 + (z + L)^2}$, and $v_r(r)$ is the (signed) rate of radius change.

At the spindle midplane ($z = 0$), these simplify by symmetry ($r_1 = r_2$):

- $v_z = dz/dt = 0$
- $v_r = dr/dt = \frac{\sqrt{r^2+L^2}}{r} \cdot v_r\left(\sqrt{r^2 + L^2}\right)$

For the decomposed velocities at the midplane:

- Velocity toward center: $v_{\text{center}} = -v_r$ (This is positive for inward motion if v_r is negative)
- Orthogonal velocity: $v_{\text{ortho}} = v_z = 0$

S4.2 Transient Model - Mean-Field Approximation

The mean-field velocity for the transient model with n force elements is:

$$\mathbf{v} = n\left(P_{\text{bound},1} v_{\text{scale},1} \hat{\mathbf{u}}_1 + P_{\text{bound},2} v_{\text{scale},2} \hat{\mathbf{u}}_2\right)$$

where $P_{\text{bound},i}$ is the steady-state probability of a single force element binding to pole i.

Saturated case:

$$P_{\text{bound},1} = P_{\text{bound},2} = \frac{k_{\text{on}}}{k_{\text{off}} + 2k_{\text{on}}}$$

Unsaturated case:
The effective binding rate to each pole, $k_{\text{bind},i}$, follows Michaelis-Menten kinetics dependent on the local microtubule density ρ_i:

$$k_{\text{bind},i} = k_{\text{on}} \frac{\rho_i}{K_m + \rho_i}$$

The steady-state probability of being bound to pole i is then given by:

$$P_{\text{bound},i} = \frac{k_{\text{bind},i}}{k_{\text{off}} + k_{\text{bind},1} + k_{\text{bind},2}}$$

where the densities ρ_i are calculated as in S3.3.

At the midplane ($z = 0$) with symmetric poles:

- Velocity toward center: $v_{\text{center}} = -v_r$
- Orthogonal velocity: $v_{\text{ortho}} = v_z = 0$

For straight filaments at $z = 0$:

$$v_{\text{center}} = \frac{2nP_{\text{bound}}v_{\text{scale}}r}{\sqrt{r^2 + L^2}}$$

The positive sign indicates inward motion toward the spindle center.

S5. Parameter Values and Justification

S5.1 Common Simulation Parameters

Table S1. Parameters common to all simulations

Parameter	Symbol	Value	Units	Description
Chromosomes per simulation	n_{chr}	920	-	Total chromosomes (46 × 20 cells)
Number of cells	n_{cells}	20	-	Simulated cell count
Output time points	$n_{\text{timepoints}}$	48	-	Matches experimental resolution
Output time step	dt	5	s	Experimental frame rate
Simulation timestep	dt_{sub}	0.01	s	Internal integration step
Half-spindle length	L	3.5	μm	Measured from experimental data
Velocity calculation window	dTV	15	s	Window for finite differences
Velocity threshold	v_{thresh}	8	μm/min	Jump artifact filter
Number of distance bins	n_{bins}	21	-	For velocity profiles

S5.2 Model-Specific Parameters

Table S2. Stable Attachment Model parameters

Parameter	Symbol	Scenario 4: Constant	Scenario 5: PEF	Units	Description
Contraction function	$v_r(r)$	-0.02	$-0.02(1 - 3e^{-r/2})$	μm/s	Sphere radius rate of change (negative for contraction)
Noise amplitude 1	σ_1	0.1	0.1	μm/$\sqrt{\text{s}}$	Radius change noise
Noise amplitude 2	σ_2	0.025	0.025	μm/$\sqrt{\text{s}}$	Position noise
PEF decay length	r_0	-	2	μm	Polar ejection force scale
PEF strength	α	-	3	-	Maximum PEF effect

Table S3. Transient Model parameters

Parameter	Symbol	Saturated (Scenarios 1,3)	Unsaturated (Scenario 2)	Units	Description
Binding rate	k_{on}	10	10	s⁻¹	Maximum binding rate
Unbinding rate	k_{off}	1	1	s⁻¹	Detachment rate
Velocity scale	v_{scale}	0.005	0.005	μm/s	Base transport velocity
Force elements	n_{int}	10	20	-	Per chromosome
Michaelis constant	K_m	0 (saturated limit)	$10^{-3.5}$	μm⁻²	Half-saturation density
Curvature	$p-2$	6 (S1), 0 (S3)	0 (straight)	-	Filament path curvature
Aspect ratio	a	1.5 (S1), 1 (S3)	1	-	Spindle shape factor
Angular distribution	$f(\theta)$	-	See Eq. S6.1	-	MT angle preference
Distribution params	κ, μ	-	7.5, $\pi/2$	-, rad	Angular sigmoid parameters

S5.3 Angular Distribution Function

The angular sigmoid distribution used for the unsaturated model is:

$$f(\theta) = \frac{\kappa(1 + \tanh[\kappa(\theta - \mu)])}{2\pi\kappa + \log\left[\cosh\left(\kappa(2\pi - \mu)\right) \cdot \text{sech}(\kappa\mu)\right]} \quad \text{(Eq. S5.1)}$$

where $\kappa = 7.5$ controls the distribution width and $\mu = \pi/2$ sets the threshold angle. This form provides smooth variation from uniform ($\kappa \to 0$) to strongly peaked ($\kappa \gg 1$) distributions for values above $\theta = \mu$, representing the preferential emission of microtubules perpendicular to the spindle axis under certain conditions.

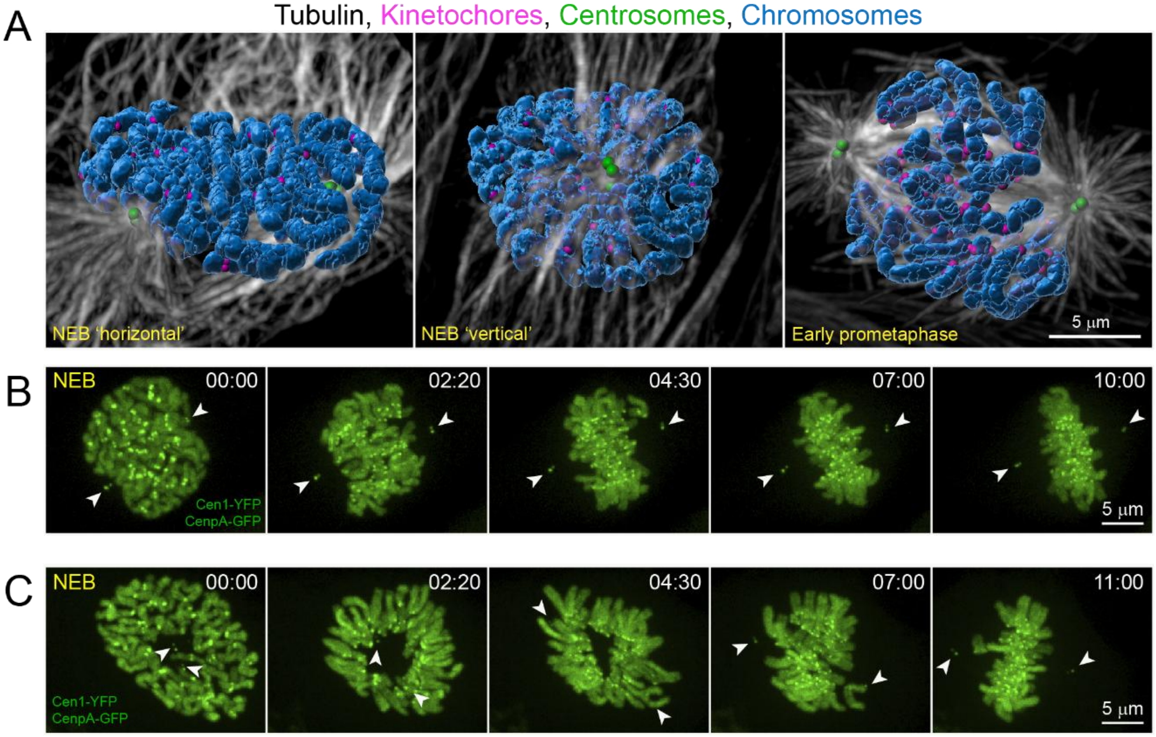

Fig. S1. Spatial distributions of chromosomes during prometaphase. (A) 3D-surface renderings of fixed RPE1 cells that express centrin1-GFP (centrosomes), CenpA-GFP (kinetochores), and immunostained for α-Tubulin (microtubules). Chromosomes are counterstained with Hoechst 33342, segmented, and surface rendered. At nuclear envelope breakdown (NEB), duplicated centrosomes reside within invaginations of the nuclear envelope on the opposite sides of the nucleus, either along its longer (NEB 'horizontal') or the shorter (NEB 'vertical') axis. In early-mid prometaphase chromosomes are not present in the immediate proximity of the centrosomes/spindle poles. (B-C) Selected time points from 4-D recordings of RPE1 cells with centrosomes separated along the longer (B) or shorter (C) axis of the nucleus at NEB. Maximum-intensity projections of the entire cell. 3D views of these cells are shown in Figure 1 C-D. Arrowheads mark centrosomes/spindle poles. Time in minutes : seconds from NEB.

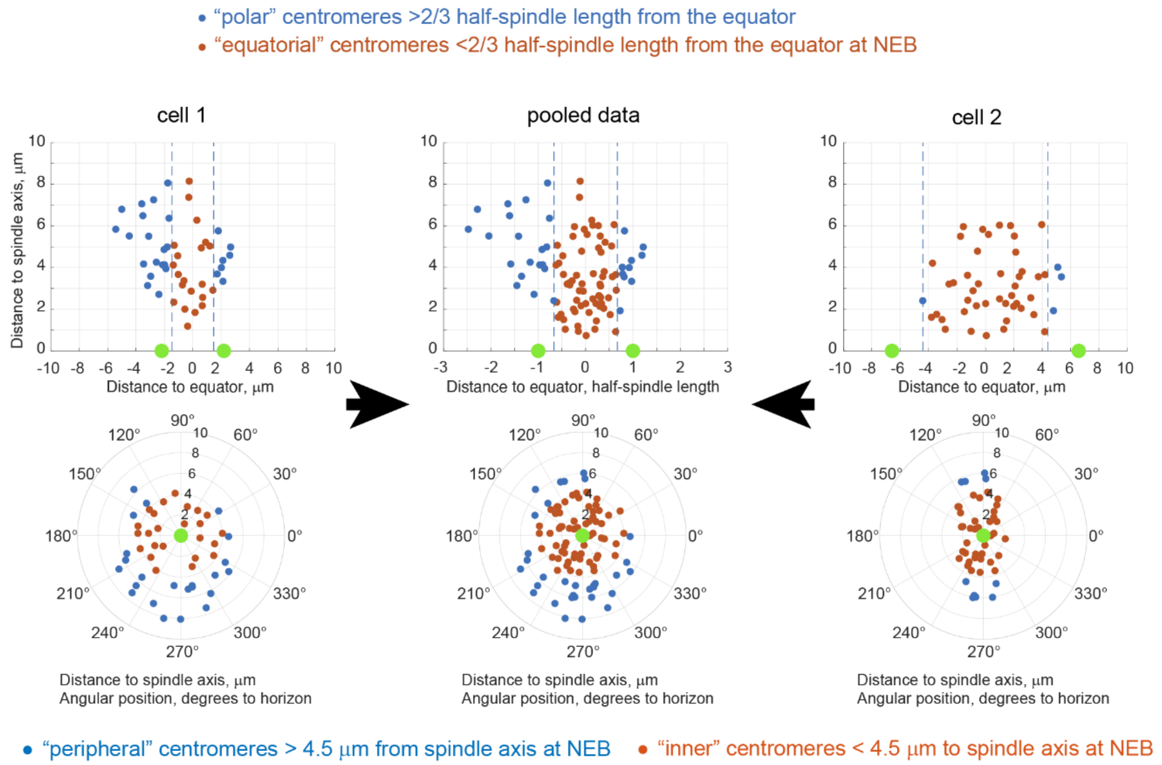

Fig. S2. Approach for quantification of centromere behavior. Centromere positions are expressed in a cylindrical coordinate system with the origin at the center of the spindle. Plots present the distance to the spindle axis (ρ) vs. the distance to the equatorial plane (Z) or the distance to the spindle axis (ρ) vs. the angular position (θ). To discriminate 'bioriented' (Z < 2/3 of the half-spindle length from the equator) vs. 'monooriented' (Z > 2/3 of the half-spindle length from the equator) chromosomes in datasets containing multiple cells, Z values are normalized to the half of the spindle length at each timepoint.

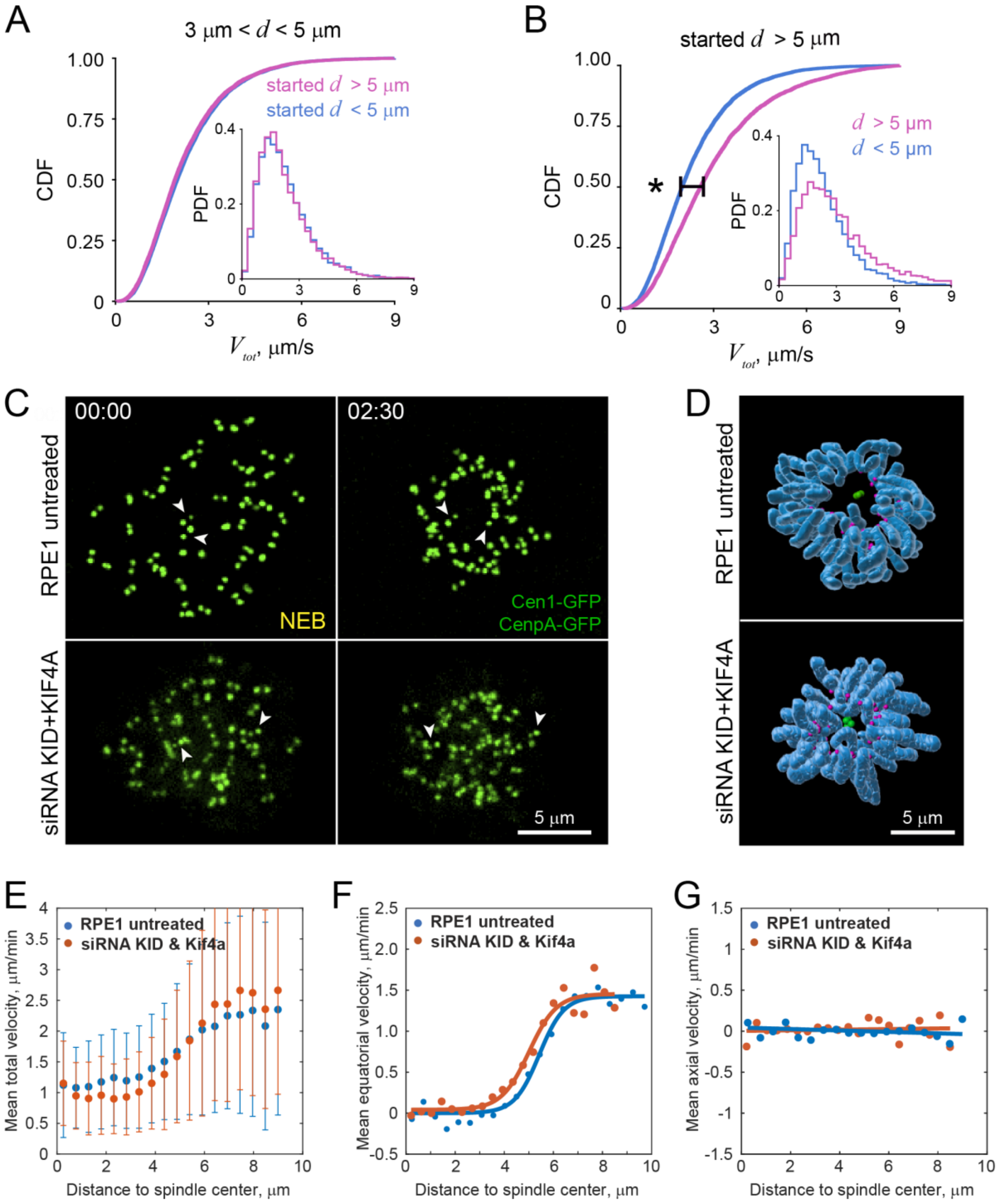

Fig. S3. Slower centromere movements are not caused by crowding within the inner parts of the spindle neither by the spindle ejection forces. (A) Cumulative distribution function (CDF) and probability density function (PDF) of velocities for centromeres initially positioned far (>5 μm, magenta) vs. closer (<5 μm, blue) from the spindle center when they move through the intermediate region of the spindle (3-5 μm from the center). No significant difference exists (two-sample *t*-test, *T* = 1.8912 and *df* = 17958). **(B)** CDF and PDF of velocities for centromeres that are initially positioned >5-μm away from the spindle center when they move through the peripheral (>5 μm from the center) vs. inner (<5 μm from the center) parts of the spindle center. Significant different (two-sample *t*-test, *T* = -32.8887 and *df* = 16812). **(C-D)** Effect of siRNA co-depletion of chromokinesins Kid and Kif4a on chromosome distribution and orientation during mid-prometaphase. Notice the presence of kinetochores near the spindle axis in the chromokinesins-depleted cell. This zone is reproducibly devoid of kinetochores in the untreated RPE1. (C) Maximum-intensity projections of the entire cell from time-lapse recordings of cells with GFP-tagged kinetochores and centrioles. Arrowheads denote centrioles. (D) Surface renderings of chromosome arms (blue) with marked positions of kinetochores (magenta) and centrioles (green). **(E)** Centromere total velocity as a function of distance to the spindle center in untreated RPE1 vs. RPE1 co-depleted for Kid and Kif4a. No significant change is observed. **(F-G)** similar to (E) but only the equatorial (F) and axial (G) components of centromere velocity are plotted. No significant differences are observed.

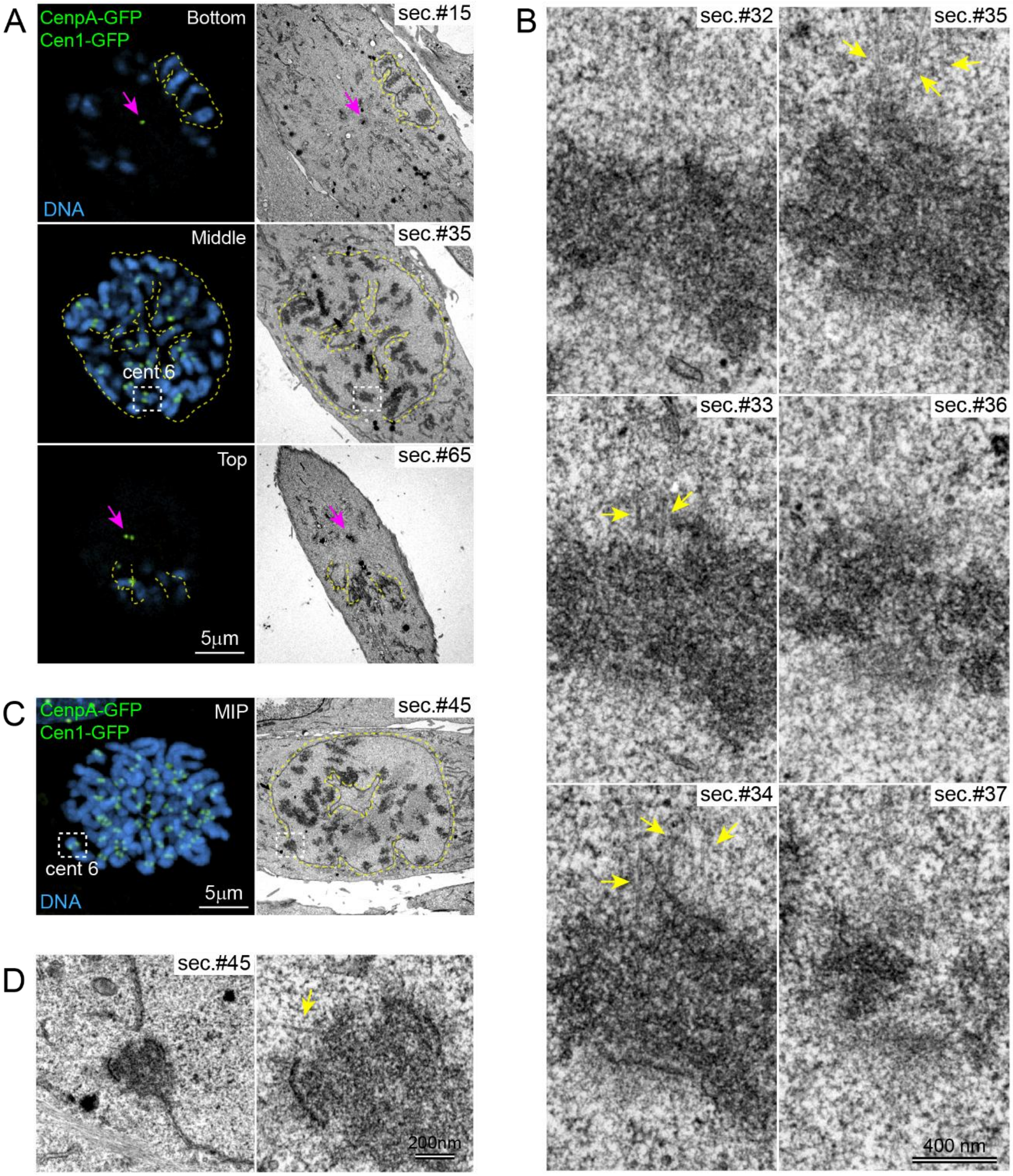

Fig. S4. Correlative Light/Electron Microscopy (CLEM) analysis of RPE1 cells fixed during nuclear envelope breakdown. (A) Selected LM planes and corresponding 80-nm EM sections of an RPE1 cell with fenestrated nuclear envelope (3-D reconstruction of this cell shown in Figure 5B). Centromeres and centrioles are tagged with CenpA-GFP and Centrin1-GFP. Chromosomes are stained with Hoechst 33342. Arrows mark centrioles, located within deep invaginations of nuclear envelope on the ventral and dorsal sides of the nucleus. Dashed yellow lines denote nuclear envelope (traced in EM sections). Discontinuities in the nuclear envelope (fenestrae) are evident in EM sections through the medial part of the cell (sec.#35). Note that the fenestrae are not adjacent to the centrosomes. Area within the dashed white box is shown in (B). (B) Serial 80-nm sections through the centromere of one chromosome (boxed in A). Arrows point at microtubules emanating from one kinetochore. No microtubule is present at the sister kinetochore. Section #34 and traces of microtubules are also shown in Figure 5C. (C) Similar to (A) but this cell was fixed at the earlier stage with just two small fenestrae forming near a small chromosome. **(D)** Higher magnifications of the centromere (cent6) adjacent to a fenestra (boxed in C) reveal a single short microtubule (arrow) near the centromere.

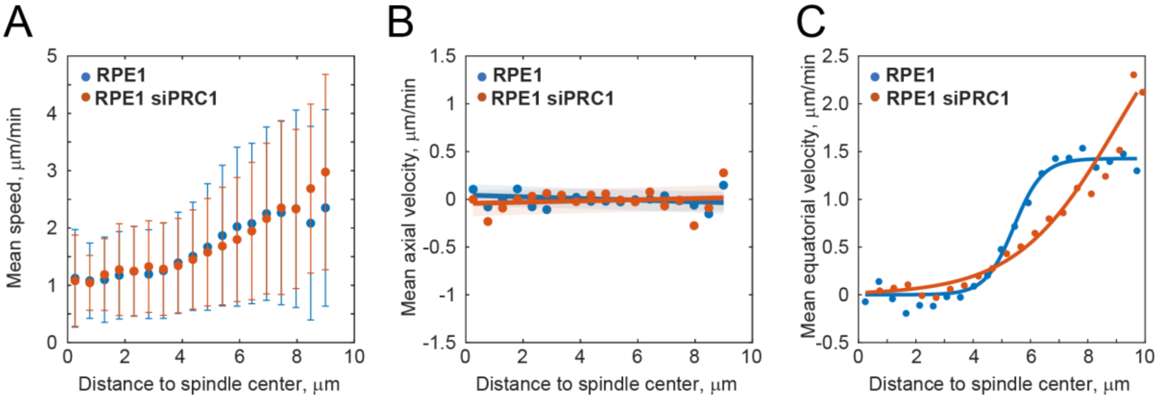

Fig. S5. Abrogation of microtubule bundling within the spindle changes relationship between centromere velocity and distance to the spindle center. (A) Centromere total velocity as a function of distance to the spindle center in untreated RPE1 vs. RPE1 depleted for PRC1 via shRNA. **(B-C)** similar to (A) but only the axial (B) and equatorial (C) components of centromere velocity are shown. Notice that equatorial velocity increases slower in between 4 and 8 μm and continues to increase at larger distances from the spindle center.